

See discussions, stats, and author profiles for this publication at: <https://www.researchgate.net/publication/221800015>

Design and Implementation of Noble Metal Nanoparticle Cluster Arrays for Plasmon Enhanced Biosensing

ARTICLE in THE JOURNAL OF PHYSICAL CHEMISTRY C · DECEMBER 2011

Impact Factor: 4.77 · DOI: 10.1021/jp207821t · Source: PubMed

CITATIONS

40

READS

159

3 AUTHORS, INCLUDING:



Svetlana V Boriskina

Massachusetts Institute of Technology

173 PUBLICATIONS 2,305 CITATIONS

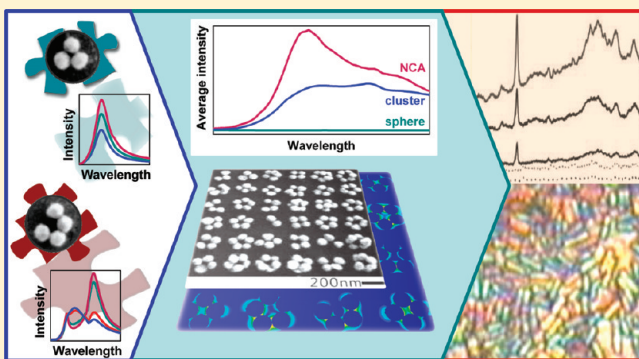
SEE PROFILE

Design and Implementation of Noble Metal Nanoparticle Cluster Arrays for Plasmon Enhanced Biosensing

Bo Yan, Svetlana V. Boriskina, and Björn M. Reinhard*

Department of Chemistry and The Photonics Center, Boston University, Boston, Massachusetts 02215, United States

ABSTRACT: Nanoparticle cluster arrays (NCAs) are a class of electromagnetic materials that comprise chemically defined nanoparticles assembled into clusters of defined size in an extended deterministic arrangement. NCAs are fabricated through integration of chemically synthesized building blocks into predefined patterns using a hybrid top-down/bottom-up fabrication approach that overcomes some of the limitations of conventional top-down fabrication methods with regard to minimum available feature size and structural complexity. NCAs can sustain near-field interactions between nanoparticles within individual clusters as well as between entire neighboring clusters. The availability of near-field interactions on multiple length scales, together with the ability to further enhance the coupled plasmon modes through photonic modes in carefully designed array morphologies, leads to a multiscale cascade electromagnetic field enhancement throughout the array. This feature article introduces the design and fabrication fundamentals of NCAs and characterizes the electromagnetic coupling mechanisms in the arrays. Furthermore, it reviews how the optical properties of NCAs can be tuned through the size and shape of the nanoparticle building blocks and the geometry, size, and separation of the assembled clusters. NCAs have potential applications in many different areas; this feature article focuses on plasmon enhanced biosensing and surface enhanced Raman spectroscopy, in particular.



fields of their LSP modes couple and generate an interparticle separation dependent spectral response of the resulting NP cluster. The dominant resonant spectral peak in NP clusters continuously red-shifts with decreasing separation,¹⁶ until at very short separations quantum plasmonic effects lead to an attenuation of the coupling interactions.¹⁷ In the case of DNA tethered 40 nm Ag nanoparticles, the onset of this transition between classical and quantum plasmonic coupling regime was observed to occur at approximately 2 nm.¹⁸ The threshold separation could, however, lie somewhat shorter for nanoparticles separated by air or another dielectric.

The interparticle separation dependent optical properties of NP dimers and larger clusters offer new opportunities for resolving subdiffraction distances between NPs targeted at specific cellular features in the optical microscope.¹⁹ We have demonstrated that plasmon coupling based imaging modalities can detect the association of laterally diffusing cell surface receptors in real-time,¹⁹ facilitate a structural characterization of cellular surfaces,²⁰ and provide spatial maps of receptor densities in plasma membranes.^{21,22}

In this Feature Article, we focus on biosensing applications that are enhanced by the intricate electromagnetic interactions between NPs in surface supported plasmonic nanostructures with tailored morphologies. It is well-known that, in addition to

I. INTRODUCTION

Noble metal nanoparticles (NPs) have fascinating photophysical properties and have been the focus of intense research since the pioneering work by Faraday¹ and Zsigmondy² more than a hundred years ago. Today we know that the optical responses of noble metal NPs are determined by their localized surface plasmon (LSP) resonances,³ which are collective coherent oscillations of the conduction band electrons in the NPs. The resonant interactions of the NPs with incident electromagnetic radiation facilitate large far-field optical cross sections.^{4,5} The exact spectral positions of LSP resonances depend on the nanoparticle material, size, shape, and refractive index of the surrounding medium.^{6–9} Spherical Au and Ag nanoparticles with diameters $d > 20$ nm, in particular, are widely used in imaging, spectroscopy, and sensing applications. They can be synthesized in large quantities with well-defined d (typical standard deviation $\sim 5\text{--}10\%$) using established wet-chemical synthesis strategies^{10–13} and can be easily detected in either darkfield or total internal reflection microscopy due to their large scattering cross sections.^{14,15} Because their signal is based on light scattering rather than fluorescence emission, NPs represent optical labels with outstanding photophysical stabilities. Their brightness, stability, and multimodal character (NPs can be imaged both in the optical and electron microscope) make NPs useful labels in bioimaging.¹⁴

Additional functionalities arise from electromagnetic interactions between individual NPs. When two or more NPs approach each other to within approximately one d , the electromagnetic

Received: August 15, 2011

Revised: October 14, 2011

Published: October 21, 2011

the prominent scattering response, strong near-field coupling between LSP resonances of closely packed NPs results in a dramatic electric field (E-field) enhancement in nanoscale volumes.²³ The enhanced E-field can amplify the efficiencies of Raman scattering, infrared (IR) absorption, and fluorescence emission processes, which culminated in the development of a range of novel sensing techniques, including surface enhanced Raman spectroscopy (SERS),²⁴ surface enhanced IR absorption spectroscopy (SEIRA),²⁵ and surface enhanced fluorescence (SEF).²⁶ These spectroscopic techniques measure intensities and frequencies of vibrational (SERS and SEIRA) or electronic (SEF) transitions and thus provide quantitative molecular signatures of great value for chemical or biological analysis.²⁷ Strong localized electromagnetic fields in NP clusters can enhance other types of nonlinear processes in a controlled fashion, for instance four-wave mixing, and could potentially facilitate local extinction measurements.²⁸

Random assemblies of colloidal particles such as fractal NP agglomerates are easy and economical to generate and can feature locations of giant E-field enhancement, so-called hot-spots.^{29,30} However, their resonance wavelengths, precise spatial locations, and field intensity values are difficult to control. Another disadvantage specific to fractal nanoparticle aggregates is the fact that their mass density, and thus the hot-spot density, decreases with increasing fractal size.³¹ Some challenging biosensing applications rely, however, on an averaging of the Raman or fluorescence signal over a relatively large area, such as an entire cell or a whole microorganism. In general, the application of SERS, SEIRA, or SEF in critical sensing fields requires nanostructured metal surfaces that combine high E-field enhancement with low on-chip and chip-to-chip variability. The fabrication of these sensors asks for rational fabrication methods that can create strongly coupled NPs of defined morphology with high structural fidelity. Since the achievable E-field intensity in coupled NPs critically depends on their separation,^{32–38} its maximization hinges on the ability to fabricate nanostructures with very narrow gaps and junctions. Conventional top-down lithographic methods, such as electron beam (e-beam) lithography or focused ion beam (FIB) techniques, show excellent reproducibility, but it remains difficult to generate structures with gaps below 10 nm. As a result, the intensities that are typically observed in lithographically fabricated nanostructures are significantly smaller compared to those achieved in clusters of nearly touching colloidal particles.

Colloidal nanoparticles can be assembled into deterministic two-dimensional (2D) arrays using DNA programmed assembly processes.^{39–41} In principle, these “chemical” fabrication techniques are promising strategies for overcoming the resolution limitations of conventional top-down fabrication approaches. In practice, DNA based fabrication approaches of plasmonic nanostructures still face many challenges. Despite recent significant advances, the efficient integration of metallic nanoparticles with $d > 20$ nm, as required for plasmonic applications, into extended arrays with well-defined morphologies remains difficult. This is partly due to the fact that the physicochemical properties of DNA attached to Au nanoparticles are significantly influenced by the presence of the particles. The development of robust fabrication strategies for DNA based plasmonic structures is complicated by the current incomplete understanding of the exact behavior of nanoparticle tethered DNA.⁴² Furthermore, the high cost of functionalized DNA oligonucleotides makes DNA based fabrication approaches elusive for many application fields.

Long-range radiative coupling between lithographically fabricated NPs arranged in periodic arrays can also boost the E-field intensity.^{43–46} Although this approach relaxes the need for very short interparticle separations, it comes at the expense of a shrinking frequency bandwidth and low spatial density of electromagnetic hot-spots. Breaking the periodicity of lithographically fabricated NP arrays offers a mechanism to manipulate their wavelength spectra,^{47–49} but this approach still faces the fundamental resolution limitations of conventional lithographic techniques and the intensity-bandwidth trade-off of photonic-plasmonic modes in NP arrays.

The need for reliable and easy-to-fabricate planar plasmonic substrates is well recognized and is reflected in significant theoretical and experimental activities aimed at developing rational design criteria and fabrication methods for NP-based structures and arrays.^{50–68} Nanoparticle cluster arrays (NCAs) are a promising electromagnetic design approach that seeks to overcome some of the limitations in conventional plasmonic structures through simultaneous control over short-(subwavelength-scale) and long-range (wavelength-scale) electromagnetic coupling. This manuscript reviews the underlying theory of the electromagnetic field enhancement in NCAs, the strategies developed for their reproducible fabrication, and their applications in sensing and spectroscopy.

II. NANOPARTICLE CLUSTER ARRAYS (NCAs): CONCEPT AND FABRICATION

We have recently introduced a combined top-down/bottom-up fabrication strategy that overcomes both the spatial-resolution limitations of e-beam lithography and the lack of NP positioning control in random colloidal NP aggregates. This approach relies on using self-assembled NP clusters as building blocks for deterministic arrays with morphologies defined by nanolithographic methods. The underlying fabrication concept is to confine NPs to predefined binding sites, where they form closely packed 2D clusters with typical separations among individual nanoparticles below 5 nm. As we describe in the following sections in more detail, the resulting NCAs are a unique class of engineered electromagnetic materials that sustain field enhancement on multiple length scales due to synergistic short- and long-range plasmon coupling in the array.

The fabrication of NCAs involves the combination of e-beam lithography and nanoparticle self-assembly (Figure 1A). Unlike in the conventional direct-write e-beam lithography, here the e-beam is not used to directly create the metal nanostructures but rather to define binding sites for colloidal NPs at specific locations. In the second fabrication step, the surface of the created binding sites is charged positively, so that in the third fabrication step negatively charged NPs can be efficiently targeted at these locations through electrostatic attraction. In the final step, the e-beam generated mask is removed to release the completed NCA. We use the e-beam to generate a mask in the first step of the NCA fabrication process, but, depending on the desired throughput and minimum intercluster separation, other top-down fabrication methods, including deep-UV lithography, nanoimprint lithography, FIB, etc., can be used to create the mask for the NCA assembly as well.

The individual steps for the NCA fabrication on a dielectric substrate using the e-beam are summarized in the following.^{69,70} A quartz or glass substrate is cleaned by standard cleaning method (Piranha clean). Then a poly(methyl methacrylate) resist layer

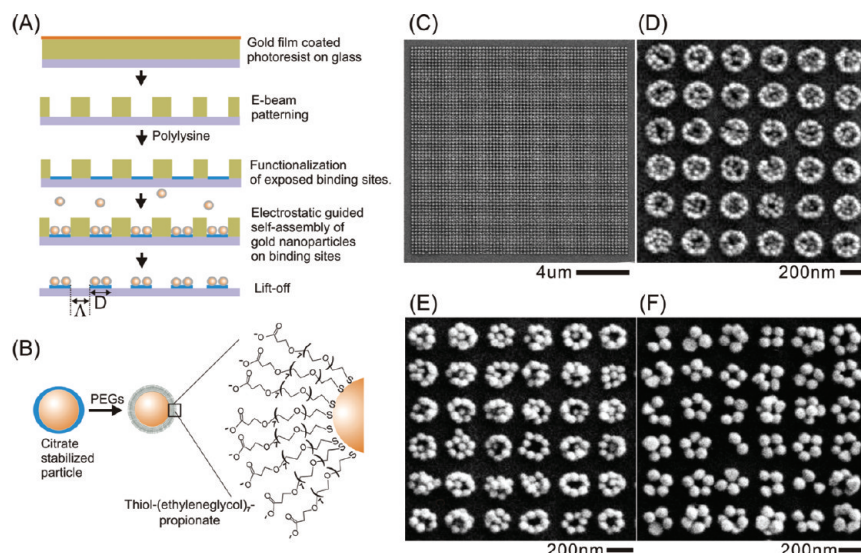


Figure 1. NCA fabrication. (A) Fabrication flowchart for NCAs (B) Au NPs used for NCA assembly are functionalized with a monolayer of short PEG molecules. (C) Overview SEM image of a resulting NCA and magnified images of NCAs assembled with (D) 40 nm, (E) 60 nm, and (F) 80 nm Au NPs. Adapted with permissions from refs 70 and 71. Copyright 2010 Wiley-VCH Verlag GmbH & Co. KGaA (ref 70). Copyright 2009 American Chemical Society (ref 71).

(PMMA) is spincoated on the substrate and baked in the oven at 170 °C for 15 min to a final thickness of ~180 nm. To make the surface conductive for e-beam lithography, a 10 nm thick Au layer is deposited on top of the PMMA layer. Subsequently, e-beam writing is performed in a Zeiss Supra 40VP scanning electron microscope equipped with an e-beam blaster. After that, the conductive Au layer is removed with Au etchant solution (Au Etch Type TFA, Transene Company Inc.) and the written pattern is developed in a methyl isobutyl ketone/isopropanol solvent mix for 70 s and rinsed with isopropanol for 20 s. Right before use, the e-beam patterned substrate is incubated with an aqueous polylysine (molecular weight 15–30 kDa) solution (2 mg/mL) for 1 h to charge the generated binding sites positively. Extra polylysine is then removed by incubating the substrate in deionized (DI) water for 5 min.

We use commercial citrate stabilized NPs (BBInternational) for the NCA assembly. The NPs are first incubated with a 10 mM aqueous solution of thiolated polyethylene glycols (PEGs; HSCH₂CH₂(OC₂H₄)₇OCH₂CH₂COOH) overnight (Figure 1B). Then, extra PEGs are removed by washing through repeated centrifugation and resuspension for three times. The PEGs serve multiple purposes. They charge the nanoparticles negatively (typical zeta-potential: -47 mV for 40 nm Au and -56 mV for 80 nm Au particles), they stabilize the nanoparticles against agglomeration during incubation with the patterned substrate, and they serve as spacers between the NPs assembled on the substrate. In the NCA self-assembly step a concentrated solution of PEG stabilized NPs (for 40 nm Au NPs: $\sim 1 \times 10^{12}$ particles/mL) in 10 mM phosphate (pH 8.6) buffer containing NaCl is incubated with the patterned substrates in a water vapor saturated atmosphere at room temperature overnight. We found that the concentration of the electrolyte, NaCl in our work, is crucial to screen the charge of the NPs on the substrate and to achieve close packed nanoparticle clusters on the binding sites. The exact concentration of NaCl needs to be adjusted depending on the size and shape of nanoparticles. For instance, we use 40 mM NaCl for $d = 40$ nm and 20 mM NaCl for $d = 80$ nm Au spheres.

After the particle binding step excess particles on the chip are washed away with DI water. The PMMA mask is finally removed through lift-off in 1-methyl-2-pyrrolidone for 5 min to release the NCA. Representative SEM images of NCAs assembled from $d = 40$ nm, 60 nm, 80 nm Au NPs using this approach are shown in Figure 1C–F.

NCAs that are intended as substrates for SERS measurements are O₂ plasma cleaned right before sample preparation to remove the PEG coating on the particle surfaces. With small modifications of the above procedure NCAs can also be generated on a thin Au film.⁷¹ Additional interactions between the LSPs of the particles and the Au film complicate, however, the analysis of the near- and far-field interactions in Au film supported NCAs, and we focus, therefore, in this article our theoretical analyses on NCAs generated on a dielectric support, unless otherwise noted.

III. NCA COLLECTIVE RESPONSE ENGINEERING

The far-field spectral properties as well as the near-field enhancement factors of NCAs are ensemble averages resulting from the synergistic interactions of NP LSP resonances on inter- and intracluster length scales. The overall performance of a NCA substrate is determined by several parameters that subdivide into “cluster” parameters (optical properties of individual NP building blocks, cluster sizes and geometries) and “array” parameters (size and morphology of the array). The formulation of rational design rules to optimize and tune the optical response of NCAs requires a quantitative understanding of how cluster and array parameters influence their optical properties. In this section, we apply a ‘bottom-up’ strategy for tailoring the near- and far-field characteristics of NCAs by investigating the effect of crucial design parameters one-by-one.

a. Elementary Building Blocks. In principle, NPs of arbitrary shape and composition can be used as elementary building blocks for 2D NCAs, provided that they can be efficiently assembled into a patterned array. We begin our analysis of the role of the building block with spherical Au^{69–72} NPs because they offer the

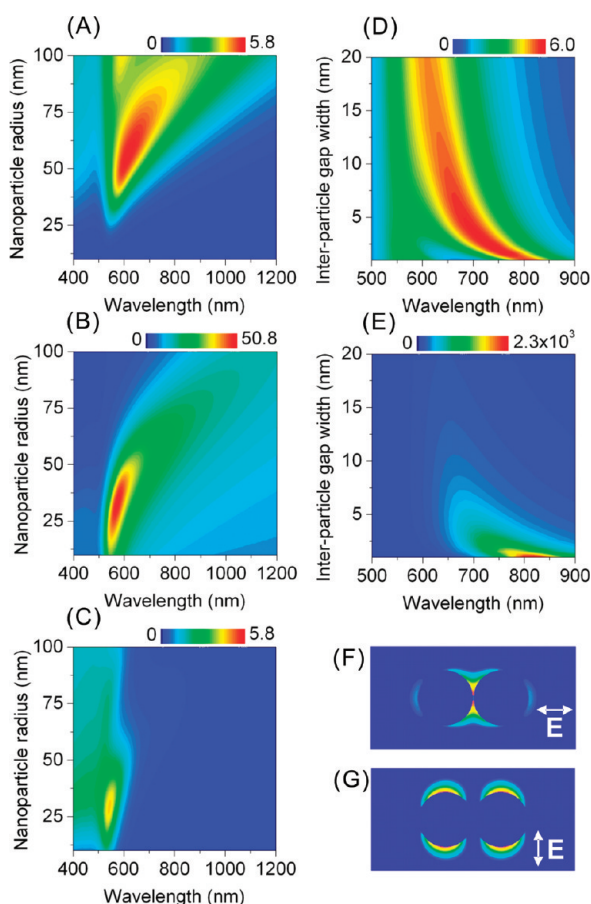


Figure 2. NCA building blocks: tuning the optical response of individual and coupled nanospheres. (A) Scattering efficiency, (B) E-field intensity enhancement, and (C) absorption efficiency of a single Au NP as function of the NP radius and wavelength under illumination by a plane wave (ambient refractive index $n_r = 1.44$). (D) Polarization-averaged scattering efficiency and (E) the near-field intensity enhancement (for the incident field polarized along the dimer axis) of an 80 nm Au NP as a function of the dimer gap width and wavelength. Spatial maps of the electric field intensity on the dimer with a 1 nm gap for the incident field polarization (F) along and (G) across the dimer axis.

highest degree of control over the cluster geometry and their electromagnetic response can be accurately predicted and tuned via electromagnetic field simulations. In particular, rigorous semianalytical solutions of Maxwell's equations for the light scattered from isolated or coupled nanospheres can be obtained by using the generalized multiparticle Mie theory (GMT).^{48,72–75} Although limited to spherical geometries, GMT, unlike more flexible ab initio numerical methods, enables physical insight into complex scenarios of LSP mode hybridization and degeneracy-splitting^{72,76,77} as well as into radiative coupling of photonic and plasmonic modes in 2D or 3D arrays of arbitrary morphology.^{48,49,78,79}

Once the NP shape is fixed, the particle sizes and interparticle separations in the clusters emerge as major design parameters that determine the NP cluster response.^{70,71} We systematically screened the influence of these parameters on the far- and near-field characteristics of the elementary building blocks in NCAs through GMT simulations (Figure 2). A comparison of the far- and near-field spectra of individual Au nanospheres (Figures 2A,B) shows that the far-field scattering efficiency (the parameter that is

typically measured when characterizing plasmonic substrates) peaks at a larger nanoparticle size than the near-field intensity enhancement, which is responsible for the plasmon enhanced spectroscopic response in SERS, SEIRA, or SEF. Consequently, one has to acknowledge that maximum scattering efficiency is not synonymous with highest near-field enhancement. In addition, one has to consider the increased dissipative losses in Au in the wavelength range below 550 nm (Figure 2C) when choosing the building blocks for NCAs. Small particles are efficient absorbers and therefore not the best candidates as NCA building blocks. If all effects are considered, nanospheres with $d = 70\text{--}80$ nm emerge as the optimal elementary building blocks that combine high field intensity with high scattering efficiency and low absorption.

Interparticle plasmon coupling is the single most important factor for boosting the near-field enhancement provided by NCAs. It has long been recognized that the width of the interparticle gaps plays an important role in shaping the far-field scattering and near-field intensity spectra of coupled NPs.^{49,74,76,77,80–83} The effect of the gap width on the optical response of the $d = 80$ nm Au nanosphere dimer is summarized in Figure 2, panels D and E; the resonance wavelength of the dominant plasmon mode red-shifts and the near-field intensity increases with decreasing gap width in the investigated range <20 nm. The near-field intensity maps for the longitudinal and transverse coupled-dipole LSP modes in Figure 2, panels F and G, emphasize that the longitudinal mode is responsible for the strong E-field localization in the dimer junction. The strong exponential dependence of the E-field intensity of the longitudinal LSP resonance on the dimer gap width^{16,18,49,84} (Figure 2E) highlights the importance of creating NP clusters with gaps below 5 nm. Gaps in this size range are difficult to realize with conventional lithographic methods, but they can be generated through the template assisted self-assembly approach in NCAs.

It should also be noted that LSP coupling efficiency and thus hot-spot intensity are reduced at very short separation due to a direct charge transfer between particles.^{17,18} We anticipate that the formations of such close contacts are avoided in NCAs due to the PEG layer on the NPs during the assembly process. We measured the thickness of the PEG layer on the NPs in solution using dynamic light scattering (DLS) to be approximately 3 nm. Since the PEGs are a soft material, the actual separation between the NPs in the clusters can be shorter than predicted by the PEG layer thickness in solution. Indeed, we find that the interparticle separations between the NP in closely packed clusters lie below the spatial resolution of our SEM (~ 5 nm). Electron microscopic studies with higher resolution are necessary to determine the exact average interparticle separation between the NPs in the assembled NCAs. Similar studies could test if it is possible to tune the average separation of the NPs in the clusters and thus to optimize the introcluster coupling interactions through the length of the used PEGs.

An experimental characterization of the near-field response of NP clusters composed of nanospheres with different d can be achieved by measuring ensemble-averaged SERS enhancement factors (G) of NCAs. G scales as the product of the E-field intensities at the pump and emission wavelengths.⁸⁵ We used para-mercaptoaniline (pMA) as a Raman marker in these measurements to quantify G since it readily chemisorbs onto Au surfaces to form a monolayer. The SERS measurements were performed in air with a Renishaw Raman microscope

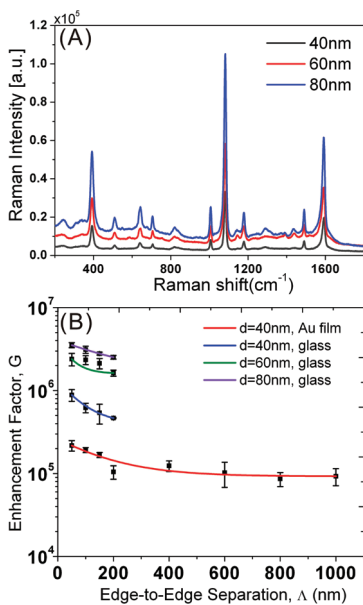


Figure 3. (A) pMA SERS spectra recorded on NCAs assembled from Au NPs with different diameters ($d = 40, 60$, and 80 nm). (B) Ensemble-averaged enhancement factor G as function of edge-to-edge separation (Λ) for NPs with different diameters (d) on glass and on glass coated with a 10 nm thin Au film. Adapted with permission from ref 70. Copyright 2010 Wiley-VCH Verlag GmbH & Co. KGaA.

(model RM-2000) or a home-built SERS microscope described in refs 69 and 86. We evaluated the SERS signal on NCAs composed of $d = 40, 60$, and 80 nm Au spheres with constant binding site diameter (D) but variable intercluster separation (Λ) fabricated on quartz. D was chosen as 200 nm . The corresponding SERS spectra obtained with an excitation wavelength of 785 nm are shown in Figure 3A.

We used the predominant peak at around 1077 cm^{-1} (α_1 C–S symmetric stretching mode) in the pMA spectra to calculate G factors for the different NCAs by comparing the signal strength measured on NCAs with that of pMA crystals. The detailed procedure of calculating G factors, which takes into account the differences in the filling fractions between the different NCAs and the number of pMA molecules attached to the Au surface, is described in ref 71. We emphasize that, although the experimentally determined, spatially averaged G factors are inevitably approximate due to simplifications and assumptions in the calculations, they still provide a useful metric to compare different SERS substrates evaluated under identical conditions.

Figure 3B summarizes the resulting $G(\Lambda)$ relationships for NCAs assembled from particles with different d . We also included the results obtained with NCAs ($D = 200 \text{ nm}$) assembled from $d = 40 \text{ nm}$ Au NPs on a 10 nm thin Au film in Figure 3B. G shows a clear Λ -dependence on all investigated NCAs, and we will analyze this trend in more detail below in section III.c. Here, we focus on the influence of d on G . Figure 3B shows that for constant Λ the ensemble-averaged enhancement factors increase with d (within the explored d range).⁷⁰ This is consistent with our theoretical predictions based on GMT simulations. Our experimental results show that the G factors for $d = 80 \text{ nm}$ and $d = 60 \text{ nm}$ are on average 5, respectively, 3.5 times higher than for $d = 40 \text{ nm}$. In addition, the comparison of the G values obtained for ($d = 40 \text{ nm}$) NCAs fabricated on quartz

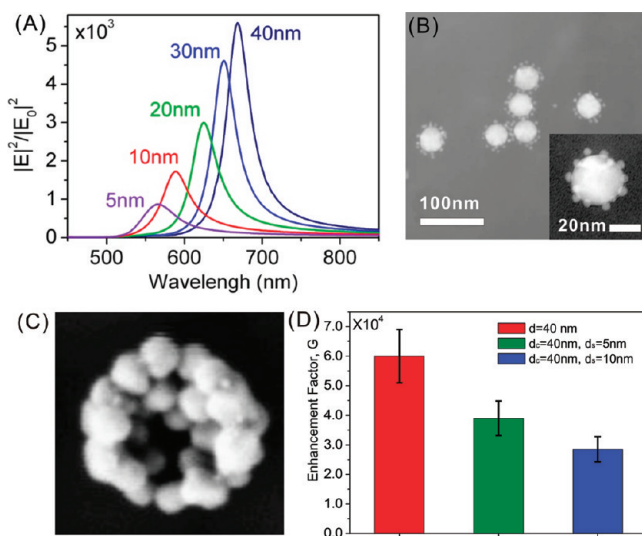


Figure 4. NCA building blocks: optical response of size-mismatched NP clusters. (A) Field intensity enhancement in the gap of an Au core–satellite dimer as a function of the satellite diameter d_s (shown as labels) and wavelength (core diameter $d_C = 40 \text{ nm}$, separation 1 nm , ambient index $n_r = 1.44$). (B) TEM image of ($d_C = 40 \text{ nm}$, $d_s = 5 \text{ nm}$) core–satellite NPs. A magnified view of an individual particle is shown in the inset. (C) SEM image of a cluster assembled from core–satellite NPs. (D) G factor comparison for NCAs assembled from $d = 40 \text{ nm}$ Au spheres, ($d_C = 40 \text{ nm}$, $d_s = 5 \text{ nm}$) core–satellite NPs, and ($d_C = 40 \text{ nm}$, $d_s = 10 \text{ nm}$) core–satellite NPs. Adapted with permission from ref 70. Copyright 2010 Wiley-VCH Verlag GmbH & Co. KGaA.

and Au shows that the Au support leads to a reduction of G by approximately a factor of 3.7.

One of the most significant advantages of template assisted self-assembly approaches over top-down fabrication strategies is that they can take advantage of the superb shape and size control offered by state-of-the-art wet-chemical synthesis methods. A wide variety of NP shapes that are difficult or impossible to generate with conventional top-down methods, such as nanostars,⁸⁷ nanourchins,⁸⁸ hollow nanoshell particles,^{83,84} or core–satellite particles,^{70,74} can be used as building blocks. The choice of such a wide range of diverse NP shapes provides additional design flexibility and spectral tunability in NCAs.

Especially core–satellite particles, in which multiple small NPs with diameter d_s are tethered to one larger core particle with diameter d_C , are intriguing building blocks for NCAs as they offer new possibilities for focusing the incident light that are missing in individual NPs. For the sake of simplicity we analyze these interactions in a dimer structure with a core particle with constant diameter ($d_C = 40 \text{ nm}$) and a satellite particle with variable diameter (d_s). The separation between the particles was fixed in our GMT simulations to 1 nm . Although this separation could be shorter than the average separation in the fabricated NCAs, the value is a reasonable choice for investigating the effect of size-mismatch in core–satellite NPs in the limit of strong coupling through classical electromagnetic simulations.

Figure 4A shows that nanodimers composed of size-mismatched nanospheres with varying diameters can be tuned to provide hot-spots across a wide frequency range. For the d_C , d_s combinations shown in Figure 4A, a decrease in size of one of the spheres results in the blue-shift and reduction of the near-field intensity peak. We note, however, that our GMT simulations predict that for some d_C , d_s combinations the peak E-field

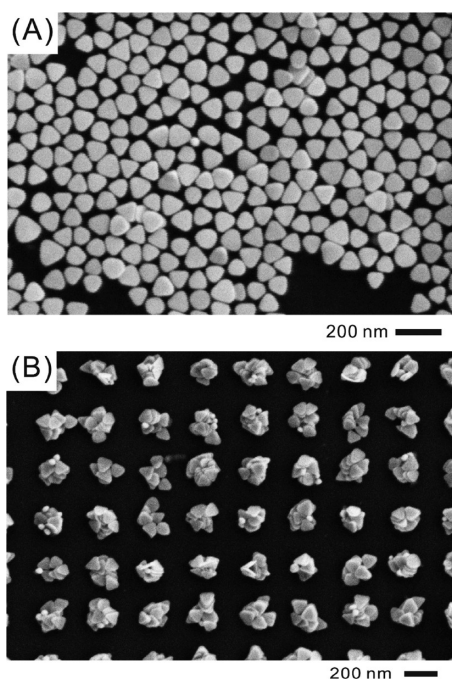


Figure 5. (A) Au nanoprisms with side length of ~ 90 nm and thickness of ~ 9 nm. (B) Nanoprism NCA with $\Lambda = 100$ nm, $D = 200$ nm.

intensities exceed those of the size-matched dimers by many folds. One example for this behavior is the combination of $d_C = 80$ nm, $d_S = 28$ nm.

We have assembled NCAs from core–satellite NPs (Figure 4, panels B and C). For the core we chose a $d_C = 40$ nm Au NP on which we assembled $d_S = 5$ and 10 nm Au NPs. The binding site diameter was chosen as $D = 200$ nm, and we used an intercluster separation of $\Lambda = 50$ nm.⁷⁰ We measured the G factor for pMA on the resulting NCAs at an excitation wavelength of 785 nm. For the constant pump-wavelength SERS measurements the theoretically predicted blue-shift in size-mismatched core–satellite NPs (when compared with clusters assembled from larger-size identical NPs) will result in the decreasing overlap of the dimer LSP resonance with the pump laser wavelength. Consistent with the predicted blue-shift, the measured SERS signal enhancements (Figure 4D) on NCAs assembled from ($d_C = 40$ nm, $d_S = 10$ nm or $d_C = 40$ nm, $d_S = 5$ nm) core–satellite NPs are lower than on NCAs assembled from spherical NCAs. We anticipate, however, that the core–satellite particles exhibit enhanced plasmonic activity in the 560–650 nm wavelength range.

Other potentially interesting building blocks for NCAs are nanoprisms. In preliminary studies we could show that these materials can be assembled into NCAs (Figure 5). Nanoprisms have a strong tendency to stack,^{89,90} and we found that the assembly conditions that lead preferentially to 2D clusters (i.e., clusters that contain only a monolayer of NPs) with spherical NPs, generate preferentially 3D clusters in the case of nanoprisms.

b. Short-Range Coupling: The Role of Nanoparticle Cluster Size and Symmetry. Another important factor governing mode coupling in NP clusters is their configuration, as defined by the number of NPs in the cluster and their spatial arrangement. The cluster configuration imposes strict limitations on the number and spectral degeneracy of hybridized LSP resonances in the clusters.^{72,91–96} The template assisted NCA self-assembly approach facilitates a systematic variation of the cluster configuration

by variation of the binding site shape and diameter. The effect of the binding site diameter (D) is illustrated in Figure 6, where we show SEM images of extracts of NCAs fabricated with constant edge-to-edge separation (Λ) but varying D (50, 80, 100, 130, and 200 nm). The images confirm that the cluster size can be continuously tuned from individual NPs to large clusters through adjustment of D ; the magnification in Figure 6F shows the hallmark of the NCAs, namely the junctions and crevices between the individual NPs in the clusters.

To investigate the influence of the cluster configuration on the far-field scattering spectra of individual NP clusters, we combined optical scattering spectroscopy with a structural characterization in the scanning electron microscope (SEM). We first generated NP clusters of defined sizes with sufficiently large intercluster separation ($\Lambda = 5 \mu\text{m}$) to avoid diffractive coupling between the individual clusters on indium tin oxide (ITO) coated glass slides. The substrate carrying the clusters was immersed in index matching glycerol ($n_r = 1.474$), sandwiched between two coverslips, and transferred in an optical microscope where they were characterized through darkfield spectroscopy. Our experimental setup for darkfield spectroscopy was based on an upright Olympus BX51WI. The samples were illuminated at oblique angle through a high numerical aperture (N.A. = 1.2–1.4) condenser using a 100 W Tungsten lamp. The light scattered from the clusters was collected with a $60\times$ oil immersion objective (N.A. = 0.65). The collected light was reimaged at the entrance port of an imaging spectrometer, which facilitated the selection of an individual cluster by adjusting the opening of the entrance slit of the spectrometer along one axis and through the software of the attached CCD camera along a second axis. The light scattered from an individual cluster was then dispersed through an appropriate grating and collected on the CCD detector. The recorded spectra were background-corrected through the light from a neighboring empty area on the substrate and corrected for the excitation profile of the Tungsten lamp by dividing through the spectrum of a whitelight scatterer. After the spectral characterization, the glycerol was removed from the samples, and the samples were transferred for inspection into the scanning electron microscope (SEM). For additional information regarding the correlation of optical spectroscopy and SEM or transmission electron microscope (TEM) characterization, please refer to Yan et al.⁷² (SEM) and Yang et al.^{18,84} (TEM).

The availability of both spectral and structural information for individual clusters enables a systematic characterization of the effect of the cluster configuration on its far-field scattering spectrum. The spectra of some selected symmetrical NP clusters assembled from $d = 60$ nm Au NPs are shown in Figure 7A; their corresponding SEM images are shown in Figure 7B–G. Overall, the recorded spectra exhibit a progressive red-shift with increasing number (n) of particles in the cluster. Furthermore, a characteristic Fano-like feature^{92,94,95,97,98} can be observed in the heptamer spectrum as a dip in the scattering intensity at approximately 820 nm. The Fano resonance results from the coupling of a superradiant bright mode (in-phase oscillation of the LSPs of the individual NPs) with a subradiant dark mode (dipolar resonance in the hexamer ring oscillating out of phase with the resonance of the central particle).

Although the recorded far-field scattering spectra of the depicted symmetrical clusters (smaller than the heptamer) are similar, their attractiveness for E-field intensity driven spectroscopic techniques can only be evaluated by comparing their near-field characteristics. The results of such comparison are summarized

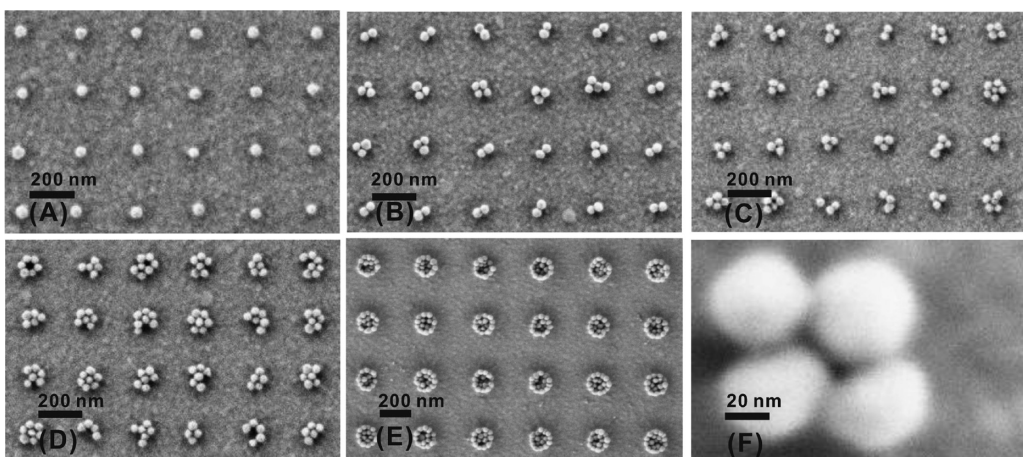


Figure 6. Collective response engineering: the role of the NP cluster size. SEM images from NCAs assembled with constant edge-to-edge separation ($\Delta = 200$ nm) but varying binding site diameter: $D = 50$ (A), 80 (B), 100 (C), 130 (D), and 200 nm (E). A magnified image of an individual cluster of 40 nm Au NPs is shown in (F). Adapted with permission from ref 71. Copyright 2009 American Chemical Society.

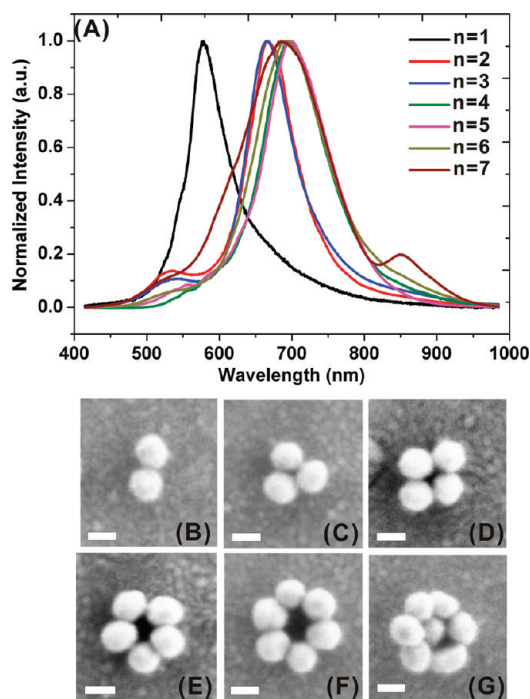


Figure 7. (A) Experimental darkfield scattering spectra of Au NP clusters with $n = 1 - 7$ (B–G) SEM images of the studied clusters. Scale bars in all SEM images indicate 50 nm. Adapted with permission from ref 72. Copyright 2011 American Chemical Society.

in Figure 8, where we plot the GMT-calculated far-field scattering (Figure 8A1–D1), and near-field intensity (Figure 8A2–D2) spectra, as well as typical on-resonance spatial E-field intensity patterns (Figure 8A3–D3) of symmetrical NP clusters of varying sizes. The simulations reproduce the experimentally observed red-shift of the far-field scattering spectrum as function of cluster size.⁷² The near-field intensity calculations reveal, however, significant differences in the performance of various symmetrical clusters. In particular, we can conclude that the symmetrical trimer and heptamer constitute exceptional NCA building blocks that provide large near-field intensity enhancements. Furthermore,

despite some peak intensity variations, their E-field intensity spectra show overall little sensitivity to the polarization of the incident light. The latter is beneficial for engineering strong collective responses since it enables all the clusters in the array to interact resonantly, independent of their location or relative geometric orientations. The hot-spot intensity spectra of symmetrical trimers and pentamers are likewise polarization-insensitive, yet are noticeably lower in intensity.

A practical advantage, especially of the trimer configuration is its simple and symmetric structure, which makes it amenable to a preferential formation in a template assisted self-assembly process using spherical binding sites. Under assembly conditions that favor dense NP packing on the exposed binding sites, the ratio of particle to binding site diameter (d/D) determines the maximum cluster size.⁷⁰ Through careful choice of D for a spherical particle with known d , it is thus feasible to preferentially form trimers. For 60 nm particles, NCAs with $D = 140$ nm are enriched in trimers. The D_{6h} heptamers are also highly symmetric and can, in principle, be templated by spherical binding sites. Because of the natural width of the d distribution in colloidal Au, NCAs always contain some variability in the cluster sizes, and the “structural scrambling” increases going from the trimer to the heptamer. Although it is possible to enrich NCAs in heptamers, the yield is lower than for the trimers. We used commercial citrate stabilized Au NPs with typical coefficients of variation of the NP diameter of $\sim 10\%$ in all our studies thus far. We anticipate that NPs with sharper size distributions will improve the cluster size selectivity of the NCA assembly approach in the future.

The low polarization sensitivity of the near-field intensity spectra observed in Figure 8 reflects the fact that the hybridized LSP modes of symmetrical NP clusters are degenerate in frequency.^{72,91,99} As illustrated in Figures 9 and 10, breaking of the cluster symmetry results in the appearance of additional resonance peaks in the cluster near- and far-field spectra due to the energy splitting of hybridized modes of various symmetries. Figure 9 shows the evolution of the measured scattering spectra of the NP trimer with the transition of the cluster configuration from D_{3h} into $D_{\infty h}$. With the increase of the trimer opening angle, its spectrum continuously evolves toward a typical spectrum of the $D_{\infty h}$ linear particle chain, which features two well-pronounced

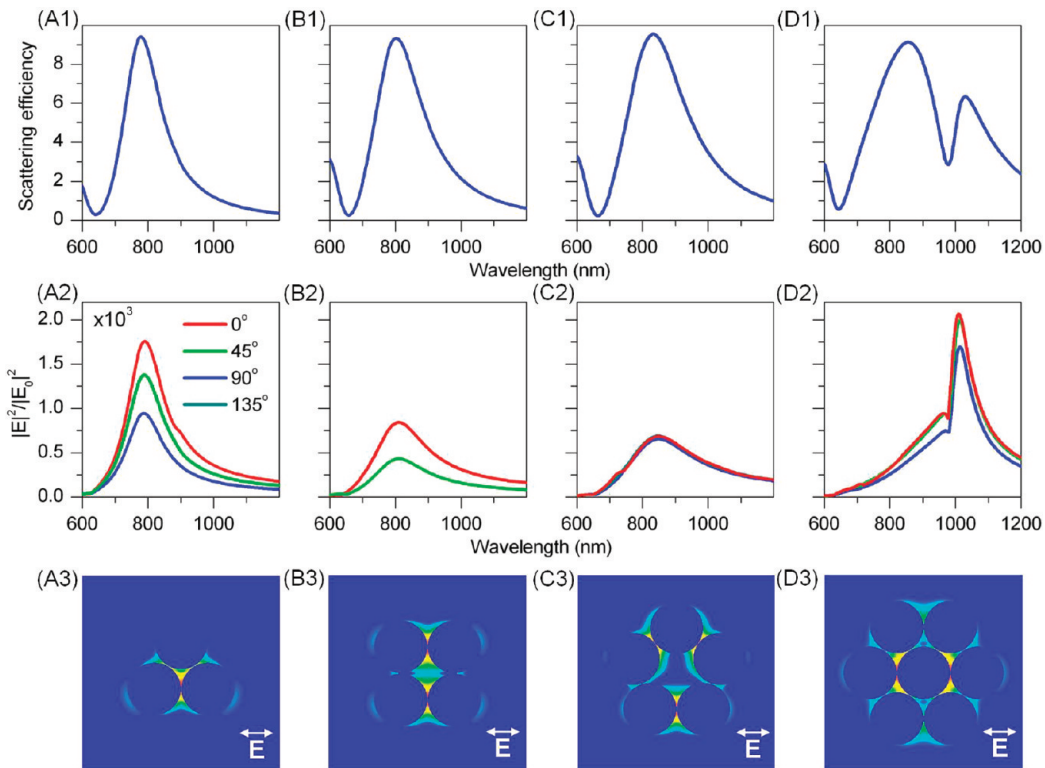


Figure 8. NCA building blocks: the role of symmetry in the NP cluster response. (A1–D1) GMT-calculated polarization-averaged scattering efficiency and (A2–D2) polarization-sensitive near-field intensity enhancement (over the free space value) spectra of symmetrical trimer (A1 and A2), tetramer (B1 and B2), pentamer (C1 and C2), and heptamer (D1 and D2) NP clusters. The clusters are composed of 80 nm-diameter Au nanospheres with 1 nm interparticle separation immersed in the ambient medium with $n_r = 1.44$ and are illuminated by a plane wave incident either normally to the cluster plane (A2–D2) or at 54° to normal (A1–D1). (A3–D3) Typical electric field intensity distributions around each cluster calculated at the wavelength of the corresponding main peak in the cluster intensity spectrum.

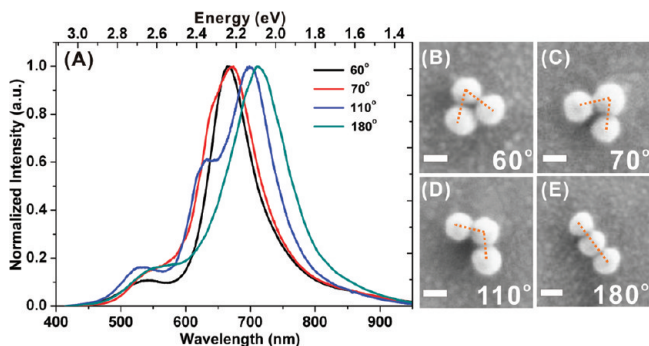


Figure 9. (A) Experimental scattering spectra and (B–E) SEM images of four individual trimers with opening angle $\alpha = 60^\circ, 70^\circ, 110^\circ$, and 180° . Scale bar denotes 50 nm in all SEM images. Adapted with permission from ref 72. Copyright 2011 American Chemical Society.

resonant peaks corresponding to the longitudinal and transverse modes of the chain.^{72,91}

In Figure 10 we compare the calculated far- (Figure 10A1–D1) and near-field (Figure 10A2–D2) frequency spectra of several asymmetrical trimers and tetramers; the corresponding on-resonance E-field intensity patterns are shown in Figure 10A3–D3. The spectra of the asymmetrical clusters feature multiple resonance peaks and strong polarization dependences. The observed wavelength selectivity and polarization sensitivity could be useful for applications that require the excitation of multiple plasmon

modes with distinct resonance peaks⁷⁹ or switching of the E-field maximum between predefined wavelengths on one chip.⁷⁸ Comparison of the near-field intensity spectra in Figures 8 and 10 reveals that the asymmetrical clusters can also generate high intensity enhancement values, comparable to those of symmetrical trimers and heptamers but at longer wavelengths (and thus off-resonance with the 785 nm pump laser used in our experiments).

In the next step, we want to complement our theoretical considerations of the E-field enhancement in specific cluster geometries with experimentally determined, ensemble-averaged SERS enhancement factors for different cluster sizes. Figure 11A illustrates how the average number of particles (n_{av}) can be tuned in NCAs by choice of the binding site diameter (D). Figure 11A also contains the cluster size distributions for the individual D values. The histograms differentiate between monomers, dimers, and trimers, whereas all larger cluster sizes are simply counted as “clusters”. We determined the G factors for different n_{av} values for pMA on NCAs that were fabricated on glass slides coated with a 10 nm thin Au film. The pump wavelength in these experiments was 785 nm, the intercluster separation was held constant at $\Lambda = 200$ nm. The obtained SERS signal enhancement as function of n_{av} is shown in Figure 11B. G initially increases strongly when the cluster size is increased from $n_{av} = 1.3$ and then peaks for $n_{av} \approx 3$ NPs in ($D = 100$ nm, $d = 40$ nm) NCAs that are enriched in D_{3h} trimers (see inset in Figure 11B). If n_{av} is further increased, the SERS signal enhancement drops again and then remains constant for larger n_{av} . This behavior is in good agreement

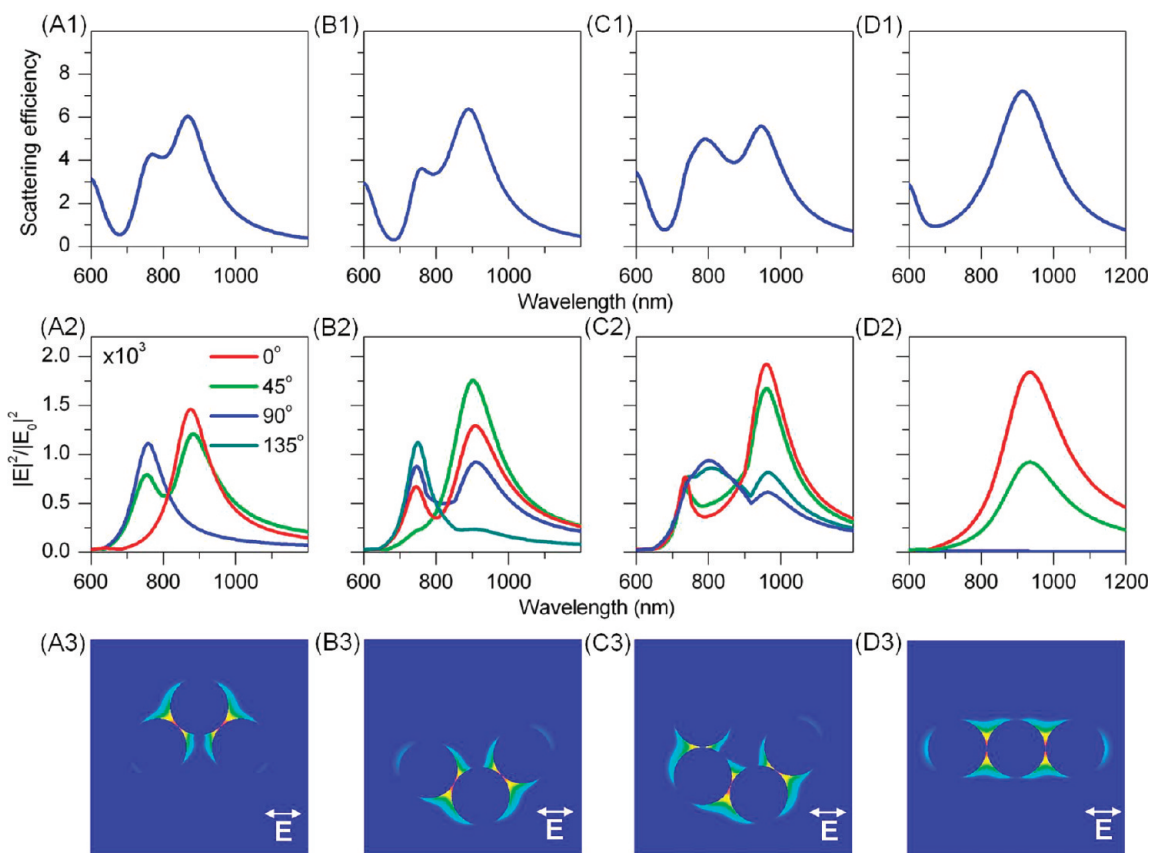


Figure 10. NCA building blocks: the role of asymmetry in the NP cluster response. (A1–D1) GMT-calculated polarization-averaged scattering efficiency and (A2–D2) polarization-sensitive electric field intensity enhancement (over the free space value) spectra of asymmetrical NP clusters: a trimer with 90° opening angle (A1 and A2), a trimer with 110° opening angle (B1 and B2), a tetramer with 108° opening angle (C1 and C2), and a linear trimer with 180° opening angle (D1 and D2). The clusters are composed of 80 nm-diameter Au nanospheres with 1 nm interparticle separation immersed in the ambient medium with $n_r = 1.44$, and are illuminated by a plane wave incident either normally to the cluster plane (A2–D2) or at 54° to normal (A1–D1). (A3–D3) Typical electric field intensity distributions around each cluster calculated at the wavelength of the corresponding main peak in the cluster E-field intensity spectrum.

with our theoretical studies, which predict the highest E-field enhancement at 785 nm in symmetrical trimers (see Figure 8). We note that the dominant peak in the heptamer E-field intensity spectrum in Figure 8 is significantly red-shifted when compared to the E-field intensity maxima of the other investigated clusters. Due to its spectral shift, the overlap of this peak with the pump wavelength is small, and the resulting SERS signal enhancement is, consequently, only moderate.

We conclude that while specific cluster geometries with $n > 4$ can provide peak E-field intensity enhancements comparable or even larger than those of clusters with $n = 3–4$, the SERS signal enhancement averaged over all cluster geometries in an NCA does not systematically increase for $n_{av} > 4$ with the pump wavelength of 785 nm. The convergence of the SERS enhancement is highlighted by the red curve in Figure 11B.

c. Electromagnetic Long-Range Correlations in NCAs. Unlike in traditional NP arrays, the electromagnetic response of periodic NCAs is determined by two characteristic separations: the interparticle separation within the clusters and the intercluster separation. The interplay of the electromagnetic coupling within and between the clusters effectively generates a multiscale SERS signal enhancement, which leads to the additional boost of the G values observed in Figure 3. The effect of the near-field coupling between interacting clusters can already

be observed in the simplest case of two NP clusters.⁷⁹ The cluster modes hybridize when the intercluster separation (L) approaches the cluster diameter (D), resulting in an increase of the near-field intensity with decreasing L . In NCAs the hybridized LSP modes of individual NP clusters can electromagnetically interact with each other to form hybridized “supermodes” that extend over the entire array. The electromagnetic coupling mechanism in the array changes when L approaches or exceeds the wavelength of light in the ambient medium. Under these conditions radiative coupling mechanisms dominate the interactions between the clusters and play a significant role in shaping the near- and far-field spectra of NCAs.^{48,79,100} Due to the existence of these synergistic interaction mechanisms, the collective NCA optical response can be tailored by tuning the intercluster separation (Λ) as well as the array morphology.⁴⁸ It becomes possible to boost the field enhancement provided by the individual clusters through electromagnetic coupling between the clusters and through coupling of photonic modes of the array with the plasmonic modes in the clusters.

Figure 12A illustrates the advantage that results from the integration of individual clusters into an array. The figure compares the spectrum of the average E-field intensity for individual isolated clusters with that of a 4×4 NCA containing the same clusters in a random arrangement with constant intercluster separation

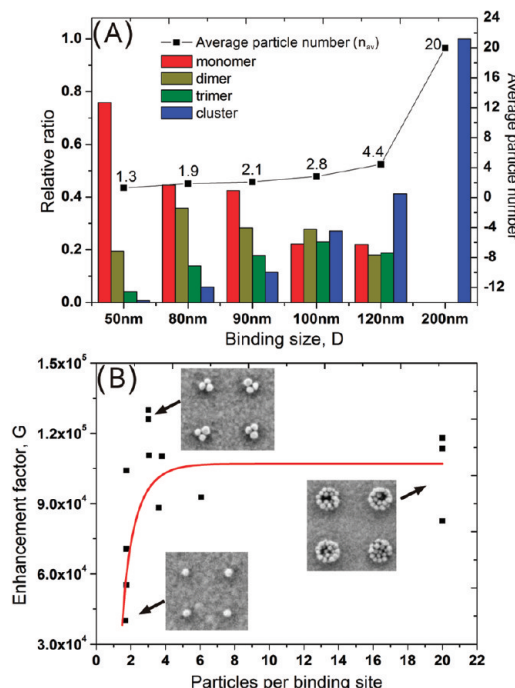


Figure 11. (A) NP cluster size distribution in NCAs with different binding site diameters ($D = 50 - 200$ nm) but constant intercluster separation ($\Lambda = 200$ nm). (B) Ensemble-averaged SERS enhancement factor (G) as a function of average cluster size (n_{av}). Adapted with permission from ref 71. Copyright 2009 American Chemical Society.

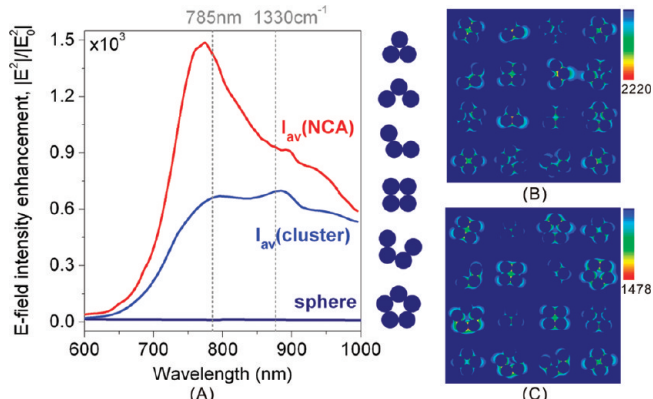


Figure 12. Collective response engineering: the role of long-range coupling in NCAs. (A) Simulated frequency spectra of the electric field intensity enhancement (over the free space value) averaged over isolated nanoparticle cluster geometries shown in the inset (blue) and clusters arranged into random 4 × 4 NCA configurations (red). The clusters are composed of 80 nm-diameter Au nanospheres with 1 nm interparticle separation immersed in the ambient medium with $n_r = 1.44$, and are illuminated by a plane wave incident normally to the cluster plane. The intensity values are averaged over various angles of the in-plane light polarization (blue and red) and over different clusters within NCAs (red). Intensity enhancement for a single 80 nm Au nanoparticle is shown for comparison (navy). (B and C) Near-field intensity distributions in a typical NCA configuration at two wavelengths: (B) 785 and (C) 876.5 nm. Adapted with permission from ref 69. Copyright 2009 American Chemical Society (ref 71).

($\Lambda = 100$ nm). The six cluster configurations chosen for this comparison are shown in the inset to Figure 12A and represent

typical cluster geometries observed in ($D = 200$ nm, $d = 80$ nm) Au NCAs (see, e.g., Figure 1F). To obtain the individual cluster spectrum (blue line), the spectra of six individual clusters were first averaged over various polarization directions of the incident light (under normal incidence to the NCA plane). In a second step, these spectra were then averaged to calculate the final spectrum. The averaged NCA spectrum (red line) was obtained in a similar fashion by averaging both over random NCA geometries built from the six cluster configurations and over different light polarizations. We also included the E-field intensity of an individual NP in Figure 12A for comparison. Figure 12, panels B and C, show the spatial near-field intensity distributions in one array configuration at the 785 nm pump wavelength and for a Stokes shift of 1330 cm⁻¹ (876.5 nm). The areas of high near-field intensity for both wavelengths show significant spatial overlap.

Figure 12A confirms that the electromagnetic coupling within the array results in an increased average E-field intensity in NCAs. Although the field enhancement can be maximized and/or tuned to a specific wavelength in optimally designed cluster arrays composed of identical units,¹⁰¹ Figure 12A confirms that the synergistic enhancement effect not only plays a positive role in NCAs composed of quasi-randomized cluster configurations but also results in the significant broadening of the NCA intensity spectra, which is beneficial for SERS applications. This result is corroborated by the experimentally observed $G(\Lambda)$ relationships for NCAs with constant D (200 nm) assembled from spherical particles with different d values. The $G(\Lambda)$ plots in Figure 3 show that for $\Lambda < 200$ nm the SERS signal enhancement increases with decreasing intercluster separation, independent of d or the substrate. We attribute this amplification of the G factors of the NP clusters in the array to an electromagnetic coupling between the hybridized LSP resonances of NP clusters once the clusters have approached each other to separations below $\Lambda \approx D$.

As already mentioned, long-range interactions between periodically positioned NP clusters in NCAs can lead to the formation of delocalized hybridized supermodes that give rise to additional bands in the scattering spectra of NCAs. The far-field scattering spectra for NCAs with constant binding site diameter ($D = 200$ nm) but variable intercluster separation ($\Lambda = [50-200]$ nm) for particles with $d = 40, 60$, and 80 nm in Figure 13 show two striking features: a high (<700 nm) energy and a low (>700 nm) energy scattering band. The high energy band (located in the gray-shaded regions in Figure 13) shows a systematic red-shift with increasing Λ until it merges with the low energy band at $\Lambda = 200$ nm. The broad low energy band arises from the NCA plasmon resonance, whereas the high energy band is assigned to an array grating resonance. Periodic arrays of Au clusters fabricated on glass act as a diffraction grating with grating constant L ($=\Lambda + D$). Diffraction at this grating is described by the grating formula $L(\sin \varphi_{inc} + \sin \theta_{det}) = (m/n_r)\lambda$, where φ_{inc} is the angle of incidence on the grating, θ_{det} is the detection angle, m the grating order, and n_r the refractive index of the surrounding. Taking into account the geometric details of the excitation and emission collection in darkfield spectroscopy, it can be shown that the high energy bands observed in Figure 13 can indeed be explained through diffraction.⁷⁰ We observed similar grating resonances and plasmon resonances in NCAs fabricated on a 10 nm thick Au film.⁷¹

To summarize, at short intercluster separations the cumulative near- and far-field optical response of NCAs is a result of the intricate interplay between near-field coupling of NPs within

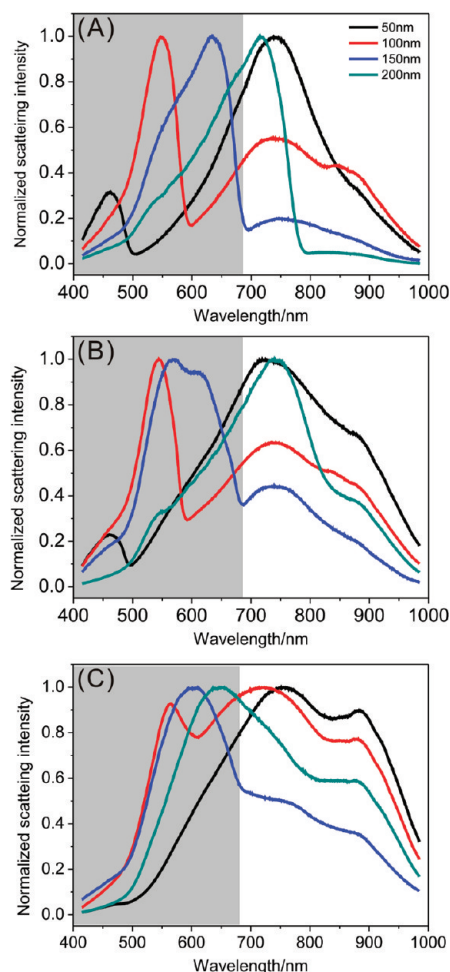


Figure 13. Far-field scattering spectra of NCAs ($D = 200$ nm) assembled with $d = 40$ (A), 60 (B), and 80 nm (C) Au NPs with intercluster separations (Λ) of 50 (black), 100 (red), 150 (blue), and 200 (turquoise) nm. The gray-shaded regions mark the high energy regions of the spectra (see text). Adapted with permission from ref 70. Copyright 2010 Wiley-VCH Verlag GmbH & Co. KGaA.

clusters and between clusters throughout the whole array. At large intercluster separations, the radiative coupling within the array becomes important so that the electromagnetic response of the NCA is determined through an interplay of near-field coupling within the clusters and radiative coupling between the clusters. All of these electromagnetic interactions are tunable in a rational fashion by variation of the building block specific (composition, d , shape) and array specific (D , Λ , morphology) NCA parameters through the introduced fabrication approaches. A synergistic combination of the different electromagnetic interaction mechanisms, aided by the developed theoretical understanding of the underlying physics, will in the future lead to a further enhancement of the NCA performance.

IV. BALANCING SIGNAL ENHANCEMENT AND REPRODUCIBILITY

In the development of high-performance plasmonic substrates for imaging and bio(chemical) sensing applications, it is equally important to provide strong signal enhancement and reproducibility. Especially in SERS, insufficient reproducibility has long

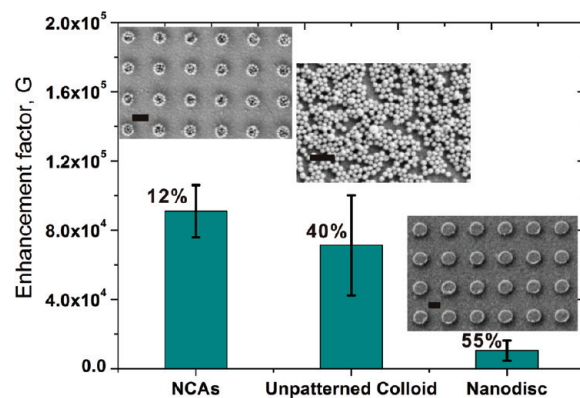


Figure 14. Comparison of ensemble-averaged SERS enhancement factors (G) of ($\Lambda = 200$ nm, $D = 200$ nm) NCAs, nonpatterned gold nanoparticle films, and periodic nanodisc arrays (edge-to-edge distance = 200 nm, disc diameter = 200 nm, disc height = 40 nm). The error bars indicate the standard deviation from 12 independent measurements on four substrates. The standard deviation as percentage of the mean and SEM images of all three substrates are included. Scale bars in all SEM images denote 200 nm. Adapted with permission from ref 71. Copyright 2009 American Chemical Society.

been a major obstacle for the application of this analytical method in critical sensing applications.^{102–104}

To evaluate the performance of NCAs with regard to these two key criteria, we benchmarked Au film supported NCAs by comparing their SERS performance with that of two competing SERS substrates: (1) 2D random (unpatterned) aggregates of 40 nm colloidal Au NPs and (2) 2D periodic arrays of Au nanodiscs fabricated by e-beam lithography.

The unpatterned monolayer of Au NPs was generated on the same substrates next to the NCAs simply by removing the photoresist from a large area in the vicinity of the surface pattern during the e-beam writing step. All subsequent processing steps were identical to those applied to the NCAs. Nanodisc arrays with the same morphology as the NCAs ($\Lambda = 200$ nm and $D = 200$ nm) were fabricated on a 10 nm thin Au film following standard procedures.^{71,105} The SERS performances of these three different substrates were then compared under identical conditions. The ensemble-averaged enhancement factors (G) for pMA (excitation wavelength: 785 nm) on the investigated substrates and their representative SEM images are summarized in Figure 14. The NCAs yield the overall highest G values, followed by the unpatterned NP substrates, and the nanofabricated nanodisc array, which showed the lowest G values.

The enhancement is higher for NCAs than for smooth nanodisc arrays due to the higher degree of roughness resulting from crevices, holes, and junctions between the NPs in the clusters and the multiscale E-field enhancement in the NCAs. The ensemble-averaged SERS enhancement factor of NCAs is also higher than those of the unpatterned Au NP substrates (2D densely packed NP monolayers, see the corresponding SEM image in Figure 14). This result comes as no surprise in view of our observation that the E-field intensity (and thus the SERS signal enhancement) peaks in isolated clusters with $n \approx 3$ and does not systematically increase with growing cluster size. Furthermore, the NCAs offer an additional mechanism for E-field enhancement and optical spectrum shaping, which is missing in the unpatterned NP substrate, namely, the intercluster coupling. This effect enables a further increase of the E-field intensity enhancement provided

by the NP clusters and, therefore, results in overall higher G values for NCAs than for the unpatterned random substrates. At $\Lambda = 200$ nm the additional gain through intercluster coupling is, however, still small.

As already mentioned, another important performance characteristic, besides the net signal enhancement, is the reproducibility of the signal enhancement generated by different plasmonic substrates. We approximated this parameter in Figure 14 as the coefficient of variation, which is the standard deviation of G values measured in 12 independent measurements on three different substrates, expressed as a percentage of the mean G value for each type of substrates. With 12% the coefficient of variation for NCAs is much smaller than for the nonpatterned colloid substrate (40%) or the periodic nanodisc arrays (55%). We note here that the overall low signal enhancement generated by evaporated nanodisc arrays results in a large coefficient of variation in their G values even though the discs have well-defined structures. We conclude that NCAs achieve a good compromise between signal enhancement and reproducibility.

V. NCA APPLICATIONS IN SENSING AND BIOSENSING

In the previous sections we have used the SERS spectra of pMA molecules to characterize the average near-field enhancement of NCAs. We have shown that the current generation of NCAs provides ensemble-averaged SERS signal enhancements of $>1 \times 10^6$ (Figure 3) and that these materials successfully combine high SERS signal enhancement and high SERS signal reproducibility (Figure 14). These advantageous performance parameters make NCAs in combination with a SERS read-out a promising analytical sensing platform that could enable a spectroscopic fingerprinting of various chemical and biological targets, ranging from individual molecules to whole cells and microorganisms. Owing to the fact that water molecules have very small Raman cross sections, SERS can be reliably applied to biological samples and samples in an aqueous environment. From the beginning, our research into NCAs was inspired by the idea of a unified SERS sensor that can detect diverse threats of chemical or biological nature at low concentrations on one chip. In the following we will review recent work that demonstrates the usefulness of NCAs in diverse SERS sensing applications.

a. Ultratrace Detection of Nitroaromatic Vapors. Nitroaromatic explosives, such as 2,4,6-trinitrotoluene (TNT), are key ingredients of several high explosives. For mine removal or the prevention of terroristic attacks, reliable and sensitive technologies for the detection of hidden or concealed high explosives are important. One approach to locate explosives is based on the detection of low concentrations of their sublimated vapor in the surrounding of the explosive material. Often these sensing schemes target the TNT contaminant 2,4-dinitrotoluol (DNT) whose vapor pressure is significantly higher than that of TNT. Although DNT is contained with less than 1% in military grade TNT, it was found that the DNT concentration is 20 times higher than that of TNT in the headspace of TNT-based landmines.¹⁰⁶ Consequently, we decided to implement an experimental strategy that maximizes the detection sensitivity for DNT through a combination of analyte enrichment and electromagnetic signal enhancement. Our aim was to achieve efficient DNT detection at ultralow concentrations in the gas-phase.⁶⁹

It is well-known that the formation of a stabilized Meisenheimer complex of DNT in a basic aqueous solution facilitates an efficient mass transfer from the gas-phase into a NaOH containing aqueous

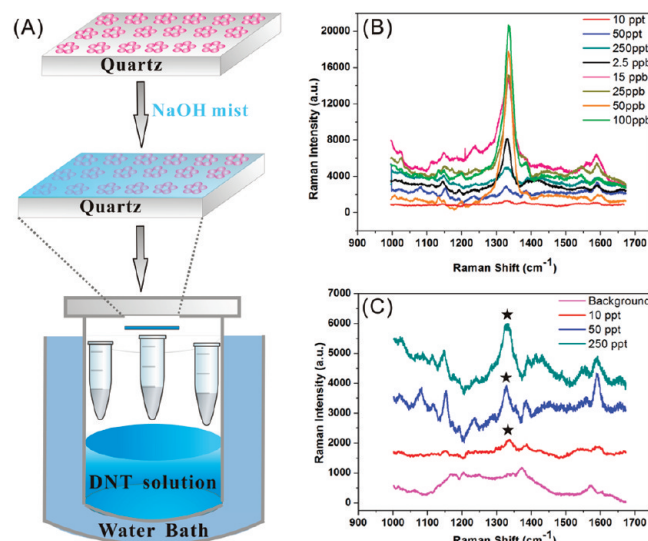


Figure 15. NCA enabled ultratrace SERS detection of DNT. (A) Experimental approach: NCAs wetted with NaOH mist are exposed to DNT vapor of a defined concentration. (B) SERS spectra of DNT exposed NCAs as function of DNT concentration (100 ppb to 10 ppt). (C) Magnification of the 150, 50, and 10 ppt spectra as well as the background. The star in panel C indicates the characteristic NO_2 stretching mode at 1336 cm^{-1} . Adapted with permission from ref 69. Copyright 2011 American Chemical Society.

film on top of a SERS substrate.^{107,108} We applied this “capture chemistry” to achieve an enrichment of DNT on ($\Lambda = 100$ nm, $D = 200$ nm, $d = 80$ nm) NCAs. In the next step, we amplified the DNT Raman signal through the NCA. Figure 15A summarizes the experimental approach for DNT detection on NCAs using SERS. Figure 15, panels B and C, shows SERS spectra of DNT at different concentrations (100 ppb to 10 ppt) in the gas-phase acquired after an incubation time of 5 min.⁶⁹ The characteristic NO_2 stretching mode of DNT at 1336 cm^{-1} is detectable even at the lowest investigated DNT concentration of 10 ppt. In most “real-world” applications the task will, however, not be to detect DNT in air but to detect DNT at low concentrations in a complex atmosphere that contains potential interferents. To evaluate the performance of NCAs under these more demanding conditions, we quantified the sensitivity of NCAs in the presence and absence of a saturated atmosphere of potential interferents, including Diesel fuel, pesticides and fertilizers.

Figure 16 shows the detected SERS intensity of the 1336 cm^{-1} band as function of DNT concentration in the presence and absence of the interferents in a double-logarithmic plot. The linear form of the SERS signal intensity vs DNT concentration (c_{DNT}) plots indicate a power-law dependence of the signal intensity on the DNT concentration. Although the presence of interferents systematically decreases the SERS signal intensity, we could still detect DNT at concentrations of 10 ppt despite the complex background. We explain the extraordinary sensitivity of our approach for DNT in the presence of the background vapors through a selective enrichment of DNT in the aqueous NaOH film on the sensor surface. The film enriches the analyte in the vicinity of the NCA but, at the same time, protects the metal surface from hydrophobic components with high vapor pressures like diesel fuel.

The detection of nitrotoluenes is not only important in the context of explosive detection. Some nitrotoluenes are human

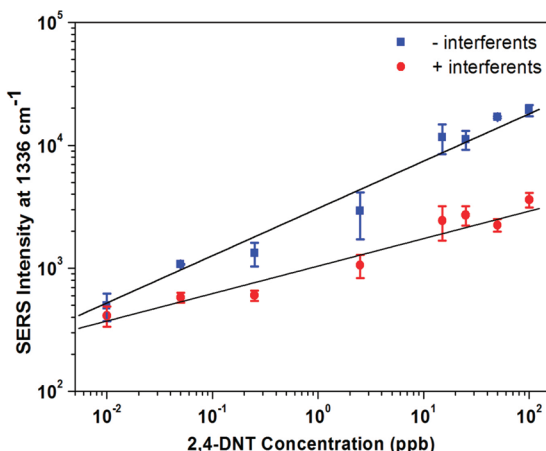


Figure 16. Peak SERS intensity of the 1336 cm^{-1} NO_2 band without (blue) and with (red) interferents (diesel, fertilizer and pesticide) as a function of DNT concentration on NaOH activated NCAs. Adapted with permission from ref 69. Copyright 2011 American Chemical Society.

carcinogens and detrimental to wildlife. There is consequently a general need for monitoring nitrotoluene concentrations in the environment, especially in industrial waste sites, soil, and groundwater. We believe that NCAs in combination with SERS are a sensor platform that is well suited for these challenging sensing tasks.

b. Bacterial Pathogen Detection and Identification. The application of NCAs in SERS sensing is not limited to small molecules. We have explored the applicability of NCAs to record spectra from entire vegetative bacterial cells. These studies were motivated by the need for the development of rapid bacteria identification modalities for optimizing treatment strategies for bacterial infections. One fundamental advantage that a SERS based approach would offer over other bacterial identification techniques is that SERS-based bacterial detection and identification relies on signal amplification. This makes the technique faster than sample amplification based techniques, such as polymerase chain reaction (PCR). For a detailed discussion of the potential advantages of SERS in microbial pathogen detection and identification we refer here to refs 109–112. In the context of this Feature Article, we focus on examining the overall experimental strategies for identifying bacterial pathogens with NCAs.

Along with high and reproducible enhancement factors, additional design criteria have to be met in the development of robust SERS substrates for bacterial pathogen detection and identification. It is, for instance, important that the bacterial cells can establish a close contact with the engineered electromagnetic hot-spots. The SERS enhancement is strongly distance dependent and an insufficient contact between the metal and the bacterial surface will prevent the acquisition of cell-specific spectra. In order to be able to average the signal over the entire cell surface, it is also important that the SERS substrate provides a homogeneous distribution of hot-spots over an area equal to or larger than the cell. The charge, the chemical composition, and the morphology of the SERS substrate all play important roles in meeting these additional requirements. The availability of a rational fabrication approach for NCAs allows a controlled adjustment of the morphology and surface properties of the SERS substrate and enables an engineering of the NCA–cell surface interactions. It is even conceivable that the ideal NCA

morphology varies for different bacterial cells depending on their size and clustering state. This would offer unique opportunities for developing selective NCA sensors that provide information about specific bacterial species.

We tested NCAs as potential biosensing substrates with two Gram-positive bacteria (*Bacillus cereus* (*B. cereus*) and *Staphylococcus aureus* (*S. aureus*)) and one Gram-negative bacterium (*Escherichia coli* (*E. coli*)). All bacteria were grown to the log phase and washed with DI water four times before drop-coating on NCAs for spectral characterization. Figure 17A shows an optical image of a monolayer of *B. cereus* on a NCA chip. SERS spectra of bacteria on NCAs were acquired using a Renishaw Raman microscope capable of $\sim 2\lambda$ spatial resolution with a 785 nm diode excitation laser. All spectra were taken with a $50\times$ objective (N.A. = 0.8) for signal collection. The illuminated area was confined to $2.5 \times 25\text{ }\mu\text{m}^2$ with an incident laser power of 4.26 mW in the sample plane. On average, 12 *B. cereus*, 80 *S. aureus*, or 62 *E. coli* cells were located in the detection area. Figure 17B shows SERS spectra from the investigated species on Au film supported NCAs ($\Lambda = 200\text{ nm}$, $D = 200\text{ nm}$, $d = 40\text{ nm}$) and nonpatterned colloid ($d = 40\text{ nm}$) substrates.⁷¹ The non-patterned Au colloids substrates were located on the same chip in close vicinity to the NCA to ensure an identical experimental condition for both measurements. The spectra in Figure 17B are representative; the NCAs provided consistently stronger SERS signals of the investigated bacteria samples than the unpatterned Au NP film. We obtained similar results as the one shown in Figure 17B with NCAs that were fabricated on glass.⁷⁰

The molecular nature of the observed spectral features in bacterial SERS spectra remains a matter of debate.^{110,113–120} We observe in samples prepared through drop-coating that NCA areas that do not contain bacteria show similar SERS signals as areas with bacteria, but that their signals are lower by a factor of 3–4. We conclude that the molecular species that give rise to the observed SERS signals colocalize with the bacteria, but that some fraction is also contained in the supernatant and thus gets distributed across the entire area of the NCA during sample preparation.⁷⁰

An important analytical question is whether the recorded SERS spectra of the individual bacteria are sufficiently characteristic to facilitate a spectroscopic identification. To verify the hypothesis that the recorded SERS spectra are vibrational fingerprints that enable to distinguish between the investigated bacterial species, we tested for systematic differences between the spectra of *B. cereus*, *S. aureus*, and *E. coli* through principal component analysis (PCA).^{121,122} PCA is a multivariate analysis strategy that transforms a set of spectra into a smaller number of uncorrelated variables called principal components (PCs). One advantage of the PCA approach is that similarities between complex spectra can be investigated in simple plots of the PC values (“score plots”) of the recorded spectra. Figure 17C shows such a score plot in the PC2-PC3 plane for the investigated bacteria recorded on ($\Lambda = 50\text{ nm}$, $D = 200\text{ nm}$, $d = 80\text{ nm}$) NCAs. The SERS spectra of the different species cluster in separated areas of the PC2-PC3 plane and are separated by more than three standard deviations from each other. This observation confirms that, at least for the investigated bacteria, the recorded spectra contain sufficient spectral differences for a robust differentiation. We note in passing that the acquisition of SERS spectra and the subsequent data analysis can be automated and accomplished in a few seconds.

So far we have only discussed SERS spectra acquired from a monolayer of cells on NCAs. We also evaluated the applicability

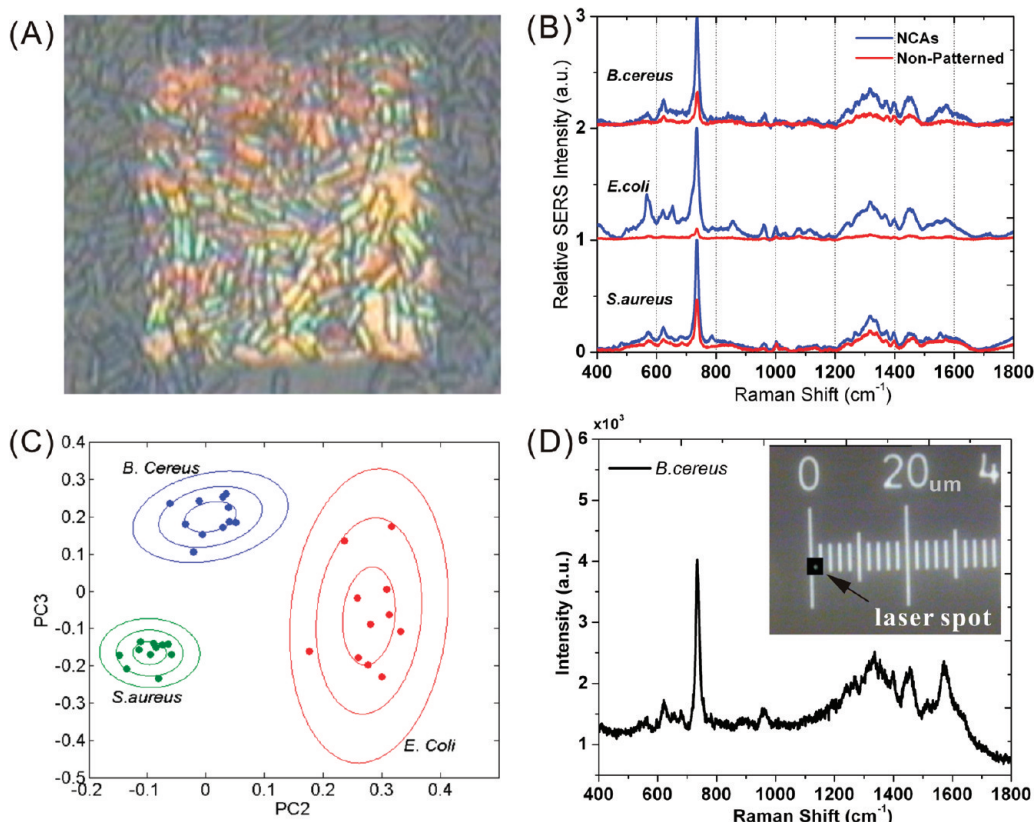


Figure 17. NCA functionality: SERS fingerprinting of bacterial pathogens using NCAs. (A) Optical image of a monolayer of *B. cereus* on a NCA chip. (B) SERS spectra of *S. aureus*, *E. coli*, and *B. cereus* recorded on NCAs (blue) and on nonpatterned Au NP films (red). (C) Score plot in the PC2-PC3 plane for *B. cereus*, *S. aureus*, and *E. coli* samples on ($\Lambda = 50$ nm, $D = 200$ nm, and $d = 80$ nm) NCAs. The rings included correspond to one, two, and three standard deviations from the cluster mean. (D) “Single bacterium SERS spectrum of *B. cereus* measured using a laser irradiated spot of $1.5\ \mu\text{m}$ in diameter at $0.03\ \text{mW}$. The inset contains an image of the laser spot. Adapted with permission from refs 70 and 71. Copyright 2010 Wiley-VCH Verlag GmbH & Co. KGaA (ref 70). Copyright 2009 American.

of NCAs for single cell measurements by reducing the irradiated sample area.⁷⁰ Using a pinhole in the laser beam path and a 100x objective we created a laser spot of $\sim 1.5\ \mu\text{m}$ diameter on a film of *B. cereus* cells on a ($\Lambda = 50$ nm, $D = 200$ nm, $d = 80$ nm) NCA. *B. cereus* cells have typical dimensions of $1\ \mu\text{m} \times 2\ \mu\text{m}$, so that on average only a single cell occupies the illuminated sample area. A representative “single” bacterium cell spectrum acquired under these conditions is shown in Figure 17D. A detailed discussion of the spectrum is given in ref.⁷⁰ In the context of this work it is sufficient to note that the performed experiments indicate that NCAs provide signal amplifications that are high enough to enable single cell SERS studies. This capability could pave the way toward spectroscopic bacterial mixture resolution in the near future.

VI. SUMMARY AND PERSPECTIVE

Nanoparticle cluster arrays (NCAs) are a class of electromagnetic materials that comprise NP clusters arranged in deterministic 2D patterns. These materials are fabricated using a template guided self-assembly approach that enables to position individual NPs or NP clusters of defined configurations at predefined locations. Since the individual building blocks are fabricated by wet-chemical synthesis, the combined top-down/bottom-up fabrication strategy enables the creation of feature sizes ranging from micrometer to chemical (subnanometer)

length scales. The template guided self-assembly approach provides a rational control over the near- and far-field responses of NCAs, which can be tuned through NP-specific parameters (size, shape, composition) and array-specific parameters (cluster size and shape, intercluster separation, spatial distribution of the clusters). In this work we have analyzed the contribution of the most relevant NCA parameters in a quantitative fashion.

NCAs sustain near-field coupling between NPs on multiple length scales (intracluster and intercluster separation), which generates a multiscale cascade field enhancement. While the average E-field enhancement of 2D NP clusters in NCAs peaks for cluster sizes of ~ 3 NPs, the multiscale E-field enhancement between the clusters provides a strategy for boosting the E-field enhancement beyond the limit of the individual clusters. Furthermore, carefully designed array morphologies can sustain interactions between clusters on longer length scales and create diffractively coupled array modes. These array modes can interact with the localized cluster modes and provide opportunities for additional E-field enhancement.

NCAs represent engineerable substrates for SERS, SEIRA, SEF, and other nonlinear spectroscopies that require a strong enhancement of the incident E-field. We have in the past focused primarily on SERS and validated that NCAs provide sufficient SERS signal enhancement to facilitate ultratrace detection of nitroaromatic components even in the presence of a complex atmosphere. We have also demonstrated that NCAs enable the

detection and identification of bacterial pathogens. Preliminary studies have shown that even single cell measurements are possible. Our bacterial studies have verified that NCAs are suitable for whole cell SERS fingerprinting studies. The SERS signal amplification is strongly distance dependent. Provided a close contact between the cell surface and the NCA is established, the information obtained in these measurements stems primarily from the cell surface and those molecules that are attached to the surface. In the future we plan to take advantage of this surface specificity to investigate mammalian cells. The cell surface plays an important role in many human diseases, most prominently cancer, and quantitative molecular information about the cell surface of healthy and cancerous cells could provide new opportunities for biomarker research. In a preliminary study we have successfully differentiated cancer from noncancer cells based on their SERS spectra.⁸⁶

NCAs are a platform technology with many potential applications beyond biosensing. The flexibility of the NCA fabrication approach makes it straightforward to adjust the electromagnetic response of NCAs. Building blocks with various optical responses can be assembled in a rational fashion to meet the specific requirements of a diverse application space, such as waveguides or light harvesting devices. The challenge for the future will be not only to expand the number of applications of the current generation of NCAs but also to explore entirely new material properties through integration of different materials (metallic and dielectric)^{123,124} and to advance the NCAs from 2D to 3D. One possible route toward 3D could utilize the beauty of wet chemistry synthesis to assemble complex 3D nanoparticles onto predesigned locations. Nanurchins, nanostars or core–satellite structures are all ideal building blocks for 3D NCAs. Another possible approach is to stack functionalized NPs on predefined binding sites using a layer-by-layer assembly method. We believe that both 2D and 3D NCAs are multiscale electromagnetic materials with great potential. Much work still lies ahead to fully utilize it.

■ AUTHOR INFORMATION

Corresponding Author

*E-mail: bmr@bu.edu.

■ BIOGRAPHIES



Bo Yan received his B.S. (2007) in Chemistry from Fudan University in Shanghai, P.R. China. He is currently a Ph.D. candidate in the group of Prof. Björn M. Reinhard at Boston

University. He has been working on the fabrication and characterization of SERS active substrate since he joined the group. His current research focuses on the spectroscopic analysis of cancerous cell surfaces.



Svetlana V. Boriskina received M.Sc. (1995) and Ph.D. (1999) degrees from Kharkov National University, Ukraine. She worked as a NATO/Royal Society Postdoctoral Fellow at University of Nottingham, U.K. (2000–2005) and a Senior Research Scientist at Kharkov National University (2005–2007) before moving to Boston University, where she is currently a Research Associate. Her research interests include nanophotonics, plasmonics, optoelectronics, metamaterials, and biosensing. Dr. Boriskina is a holder of the 2007 Joint Award of the International Commission for Optics and the Abdus Salam International Centre for Theoretical Physics, a senior member of the Institute of Electrical and Electronics Engineers, and a member of the Optical Society of America.



Björn M. Reinhard is an Assistant Professor of Chemistry and the Director of the Nano-Bio Interface Laboratory of the Photonics Center at Boston University. He earned his Ph.D. in Chemistry in 2003 at the Technical University Kaiserslautern, Germany. After a postdoctoral stay at the University of California at Berkeley, he joined Boston University in 2007. His research interests include fundamental aspects of photonic and plasmonic nanomaterials as well as their integration into enabling tools for investigating living systems and cellular processes.

■ ACKNOWLEDGMENT

The work was partially supported by the National Institutes of Health through Grant No. 5R01CA138509-03 and the National

Science Foundation through Grant Nos. CBET-0853798 and CBET-0953121.

■ REFERENCES

- (1) Faraday, M. *Philos. Trans. R. Soc. London* **1857**, *147*, 145–181.
- (2) Zsigmondy, R. *Justus Liebigs Ann. Chem.* **1898**, *301*, 29–54.
- (3) Kreibig, U.; Vollmer, M. *Optical properties of metal clusters*; Springer: Berlin, 1995.
- (4) Yguerabide, J.; Yguerabide, E. E. *Anal. Biochem.* **1998**, *262*, 157–176.
- (5) Yguerabide, J.; Yguerabide, E. E. *Anal. Biochem.* **1998**, *262*, 137–156.
- (6) Henry, A. I.; Bingham, J. M.; Ringe, E.; Marks, L. D.; Schatz, G. C.; Van Duyne, R. P. *J. Phys. Chem. C* **2011**, *115*, 9291–9305.
- (7) Kelly, K. L.; Coronado, E.; Zhao, L. L.; Schatz, G. C. *J. Phys. Chem. B* **2003**, *107*, 668–677.
- (8) Link, S.; El-Sayed, M. A. *Annu. Rev. Phys. Chem.* **2003**, *54*, 331–366.
- (9) Sherry, L. J.; Chang, S. H.; Schatz, G. C.; Van Duyne, R. P.; Wiley, B. J.; Xia, Y. N. *Nano Lett.* **2005**, *5*, 2034–2038.
- (10) Brust, M.; Walker, M.; Bethell, D.; Schiffrin, D. J.; Whyman, R. *J. Chem. Soc., Chem. Commun.* **1994**, 801–802.
- (11) Kimling, J.; Maier, M.; Okenve, B.; Kotaidis, V.; Ballot, H.; Plech, A. *J. Phys. Chem. B* **2006**, *110*, 15700–15707.
- (12) Rodriguez-Fernandez, J.; Perez-Juste, J.; Javier Garcia de Abajo, F.; Liz-Marzan, L. M. *Langmuir* **2006**, *22*, 7007–7010.
- (13) Ziegler, C.; Eychmueller, A. *J. Phys. Chem. C* **2011**, *115*, 4502–4506.
- (14) Schultz, S.; Smith, D. R.; Mock, J. J.; Schultz, D. A. *Proc. Natl. Acad. Sci. U.S.A.* **2000**, *97*, 996–1001.
- (15) Sonnichsen, C.; Geier, S.; Hecker, N. E.; von Plessen, G.; Feldmann, J.; Ditzbacher, H.; Lamprecht, B.; Krenn, J. R.; Ausseneegg, F. R.; Chan, V. Z. H.; et al. *Appl. Phys. Lett.* **2000**, *77*, 2949–2951.
- (16) Reinhard, B. M.; Siu, M.; Agarwal, H.; Alivisatos, A. P.; Liphardt, J. *Nano Lett.* **2005**, *5*, 2246–2252.
- (17) Zuloaga, J.; Prodan, E.; Nordlander, P. *Nano Lett.* **2009**, *9*, 887–891.
- (18) Yang, L. L.; Wang, H. Y.; Yan, B.; Reinhard, B. M. *J. Phys. Chem. C* **2010**, *114*, 4901–4908.
- (19) Rong, G. X.; Wang, H. Y.; Skewis, L. R.; Reinhard, B. M. *Nano Lett.* **2008**, *8*, 3386–3393.
- (20) Rong, G. X.; Wang, H. Y.; Reinhard, B. M. *Nano Lett.* **2010**, *10*, 230–238.
- (21) Wang, H.; Rong, G.; Yan, B.; Yang, L.; Reinhard, B. M. *Nano Lett.* **2011**, *11*, 498–504.
- (22) Wang, J.; Boriskina, S. V.; Wang, H.; Reinhard, B. M. *ACS Nano* **2011**, *8*, 6619–6628.
- (23) Markel, V. A.; Shalaev, V. M.; Zhang, P.; Huynh, W.; Tay, L.; Haslett, T. L.; Moskovits, M. *Phys. Rev. B* **1999**, *59*, 10903–10909.
- (24) Jeanmaire, D. L.; Vanduyne, R. P. *J. Electroanal. Chem.* **1977**, *84*, 1–20.
- (25) Hartstein, A.; Kirtley, J. R.; Tsang, J. C. *Phys. Rev. Lett.* **1980**, *45*, 201–204.
- (26) Lakowicz, J. R. *Anal. Biochem.* **2005**, *337*, 171–194.
- (27) Kneipp, J.; Kneipp, H.; Kneipp, K. *Chem. Soc. Rev.* **2008**, *37*, 1052–1060.
- (28) Palomba, S.; Danckwerts, M.; Novotny, L. *J. Opt. A-Pure Appl. Opt.* **2009**, *11*, 114030.
- (29) Shalaev, V. M.; Botet, R.; Tsai, D. P.; Kovacs, J.; Moskovits, M. *Phys. A* **1994**, *207*, 197–207.
- (30) Stockman, M. I.; Shalaev, V. M.; Moskovits, M.; Botet, R.; George, T. F. *Phys. Rev. B* **1992**, *46*, 2821–2830.
- (31) Christensen, K.; Molonev, N. R. *Complexity and criticality*; Imperial College Press: London, 2005.
- (32) Elghanian, R.; Storhoff, J. J.; Mucic, R. C.; Letsinger, R. L.; Mirkin, C. A. *Science* **1997**, *277*, 1078–1081.
- (33) Hao, E.; Schatz, G. C. *J. Chem. Phys.* **2004**, *120*, 357–366.
- (34) Jiang, J.; Bosnick, K.; Maillard, M.; Brus, L. *J. Phys. Chem. B* **2003**, *107*, 9964–9972.
- (35) Larkin, I. A.; Stockman, M. I.; Achermann, M.; Klimov, V. I. *Phys. Rev. B* **2004**, *69*.
- (36) Michaels, A. M.; Jiang, J.; Brus, L. *J. Phys. Chem. B* **2000**, *104*, 11965–11971.
- (37) Su, K. H.; Wei, Q. H.; Zhang, X.; Mock, J. J.; Smith, D. R.; Schultz, S. *Nano Lett.* **2003**, *3*, 1087–1090.
- (38) Xu, H. X.; Aizpurua, J.; Kall, M.; Apell, P. *Phys. Rev. E* **2000**, *62*, 4318–4324.
- (39) Lalander, C. H.; Zheng, Y.; Dhuey, S.; Cabrini, S.; Bach, U. *ACS Nano* **2010**, *4*, 6153–6161.
- (40) Le, J. D.; Pinto, Y.; Seeman, N. C.; Musier-Forsyth, K.; Taton, T. A.; Kiehl, R. A. *Nano Lett.* **2004**, *4*, 2343–2347.
- (41) Xiao, S. J.; Liu, F. R.; Rosen, A. E.; Hainfeld, J. F.; Seeman, N. C.; Musier-Forsyth, K.; Kiehl, R. A. *J. Nanopart. Res.* **2002**, *4*, 313–317.
- (42) Lee, O.-S.; Prytkova, T. R.; Schatz, G. C. *J. Phys. Chem. Lett.* **2010**, *1*, 1781–1788.
- (43) Adato, R.; Yanik, A. A.; Amsden, J. J.; Kaplan, D. L.; Omenetto, F. G.; Hong, M. K.; Erramilli, S.; Altug, H. *Proc. Natl. Acad. Sci. U.S.A.* **2009**, *106*, 19227–19232.
- (44) Chu, Y.; Schonbrun, E.; Yang, T.; Crozier, K. B. *Appl. Phys. Lett.* **2008**, *93*.
- (45) Zou, S. L.; Schatz, G. C. *Chem. Phys. Lett.* **2005**, *403*, 62–67.
- (46) Zou, S. L.; Schatz, G. C. *Surf. Enhanced Raman Scattering: Phys. Appl.* **2006**, *103*, 67–85.
- (47) Forestiere, C.; Miano, G.; Boriskina, S. V.; Dal Negro, L. *Opt. Express* **2009**, *17*, 9648–9661.
- (48) Gopinath, A.; Boriskina, S. V.; Feng, N. N.; Reinhard, B. M.; Dal Negro, L. *Nano Lett.* **2008**, *8*, 2423–2431.
- (49) Gopinath, A.; Boriskina, S. V.; Reinhard, B. M.; Dal Negro, L. *Opt. Express* **2009**, *17*, 3741–3753.
- (50) Abu Hatab, N. A.; Oran, J. M.; Sepaniak, M. J. *ACS Nano* **2008**, *2*, 377–385.
- (51) Anema, J. R.; Brolo, A. G.; Marthandam, P.; Gordon, R. *J. Phys. Chem. C* **2008**, *112*, 17051–17055.
- (52) Bahns, J. T.; Imre, A.; Vlasko-Vlasov, V. K.; Pearson, J.; Hiller, J. M.; Chen, L. H.; Welp, U. *Appl. Phys. Lett.* **2007**, *91*.
- (53) Cerf, A.; Molnar, G.; Vieu, C. *ACS Appl. Mater. Interfaces* **2009**, *1*, 2544–2550.
- (54) Ebbesen, T. W.; Lezec, H. J.; Ghaemi, H. F.; Thio, T.; Wolff, P. A. *Nature* **1998**, *391*, 667–669.
- (55) Fan, M. K.; Andrade, G. F. S.; Brolo, A. G. *Anal. Chim. Acta* **2011**, *693*, 7–25.
- (56) Guieu, V.; Lagugne-Labarthe, F.; Servant, L.; Talaga, D.; Sojic, N. *Small* **2008**, *4*, 96–99.
- (57) Hankus, M. E.; Li, H.; Gibson, G. J.; Cullum, B. M. *Anal. Chem.* **2006**, *78*, 7535–7546.
- (58) Haynes, C. L.; Van Duyne, R. P. *J. Phys. Chem. B* **2001**, *105*, 5599–5611.
- (59) Haynes, C. L.; Van Duyne, R. P. *J. Phys. Chem. B* **2003**, *107*, 7426–7433.
- (60) Im, H.; Bantz, K. C.; Lindquist, N. C.; Haynes, C. L.; Oh, S.-H. *Nano Lett.* **2010**, *10*, 2231–2236.
- (61) Kahl, M.; Voges, E.; Kostrewa, S.; Viets, C.; Hill, W. *Sens. Actuators, B* **1998**, *51*, 285–291.
- (62) Stokes, D. L.; Chi, Z. H.; Vo-Dinh, T. *Appl. Spectrosc.* **2004**, *58*, 292–298.
- (63) Theiss, J.; Pavaskar, P.; Echternach, P. M.; Muller, R. E.; Cronin, S. B. *Nano Lett.* **2010**, *10*, 2749–2754.
- (64) Wang, Y.; Becker, M.; Wang, L.; Liu, J.; Scholz, R.; Peng, J.; Goesele, U.; Christiansen, S.; Kim, D. H.; Steinhart, M. *Nano Lett.* **2009**, *9*, 2384–2389.
- (65) White, D. J.; Stoddart, P. R. *Opt. Lett.* **2005**, *30*, 598–600.
- (66) Xie, F.; Drozdowicz-Tomsia, K.; Goldys, E. M. *Chem. Phys. Lett.* **2008**, *466*, 186–188.
- (67) Yu, Q.; Guan, P.; Qin, D.; Golden, G.; Wallace, P. M. *Nano Lett.* **2008**, *8*, 1923–1928.
- (68) Perney, N. M. B.; de Abajo, F. J. G.; Baumberg, J. J.; Tang, A.; Netti, M. C.; Charlton, M. D. B.; Zoorob, M. E. *Phys. Rev. B* **2007**, *76*, 035426.
- (69) Wang, J.; Yang, L. L.; Boriskina, S.; Yan, B.; Reinhard, B. M. *Anal. Chem.* **2011**, *83*, 2243–2249.

- (70) Yang, L.; Yan, B.; Premasiri, W. R.; Ziegler, L. D.; Dal Negro, L.; Reinhard, B. M. *Adv. Funct. Mater.* **2010**, *20*, 2619–2628.
- (71) Yan, B.; Thubagere, A.; Premasiri, W. R.; Ziegler, L. D.; Dal Negro, L.; Reinhard, B. M. *ACS Nano* **2009**, *3*, 1190–1202.
- (72) Yan, B.; Boriskina, S. V.; Reinhard, B. M. *J. Phys. Chem. C* **2011**, *115*, 4578–4583.
- (73) Mackowski, D. W. *J. Opt. Soc. Am. A* **1994**, *11*, 2851–2861.
- (74) Pellegrini, G.; Mattei, G.; Bello, V.; Mazzoldi, P. *Mater. Sci. Eng., C Biol. Sci.* **2007**, *27*, 1347–1350.
- (75) Xu, Y. L. *Appl. Opt.* **1995**, *34*, 4573–4588.
- (76) Bek, A.; Jansen, R.; Ringler, M.; Mayilo, S.; Klar, T. A.; Feldmann, J. *Nano Lett.* **2008**, *8*, 485–490.
- (77) Nordlander, P.; Oubre, C.; Prodan, E.; Li, K.; Stockman, M. I. *Nano Lett.* **2004**, *4*, 899–903.
- (78) Boriskina, S. V.; Dal Negro, L. *Opt. Lett.* **2010**, *35*, 538–540.
- (79) Gopinath, A.; Boriskina, S. V.; Premasiri, W. R.; Ziegler, L.; Reinhard, B. M.; Dal Negro, L. *Nano Lett.* **2009**, *9*, 3922–3929.
- (80) Alexander, K. D.; Skinner, K.; Zhang, S. P.; Wei, H.; Lopez, R. *Nano Lett.* **2010**, *10*, 4488–4493.
- (81) Huang, F. M.; Baumberg, J. J. *Nano Lett.* **2010**, *10*, 1787–1792.
- (82) Rechberger, W.; Hohenau, A.; Leitner, A.; Krenn, J. R.; Lamprecht, B.; Aussenegg, F. R. *Opt. Commun.* **2003**, *220*, 137–141.
- (83) Talley, C. E.; Jackson, J. B.; Oubre, C.; Grady, N. K.; Hollars, C. W.; Lane, S. M.; Huser, T. R.; Nordlander, P.; Halas, N. J. *Nano Lett.* **2005**, *5*, 1569–1574.
- (84) Yang, L. L.; Yan, B.; Reinhard, B. M. *J. Phys. Chem. C* **2008**, *112*, 15989–15996.
- (85) Le Ru, E. C.; Etchegoin, P. G. *Chem. Phys. Lett.* **2006**, *423*, 63–66.
- (86) Yan, B.; Reinhard, B. M. *J. Phys. Chem. Lett.* **2010**, *1*, 1595–1598.
- (87) Khouri, C. G.; Vo-Dinh, T. *J. Phys. Chem. C* **2008**, *112*, 18849–18859.
- (88) Bakr, O. M.; Wunsch, B. H.; Stellacci, F. *Chem. Mater.* **2006**, *18*, 3297–3301.
- (89) Bae, Y.; Kim, N. H.; Kim, M.; Lee, K. Y.; Han, S. W. *J. Am. Chem. Soc.* **2008**, *130*, 5432–5433.
- (90) Jin, R. C.; Cao, Y. C.; Hao, E. C.; Metraux, G. S.; Schatz, G. C.; Mirkin, C. A. *Nature* **2003**, *425*, 487–490.
- (91) Chuntonov, L.; Haran, G. *Nano Lett.* **2011**, *11*, 2440–2445.
- (92) Hentschel, M.; Dregely, D.; Vogelgesang, R.; Giessen, H.; Liu, N. *ACS Nano* **2011**, *5*, 2042–2050.
- (93) Hentschel, M.; Saliba, M.; Vogelgesang, R.; Giessen, H.; Alivisatos, A. P.; Liu, N. *Nano Lett.* **2010**, *10*, 2721–2726.
- (94) Lassiter, J. B.; Sobhani, H.; Fan, J. A.; Kundu, J.; Capasso, F.; Nordlander, P.; Halas, N. J. *Nano Lett.* **2010**, *10*, 3184–3189.
- (95) Mirin, N. A.; Bao, K.; Nordlander, P. *J. Phys. Chem. A* **2009**, *113*, 4028–4034.
- (96) Rahmani, M.; Tahmasebi, T.; Lin, Y.; Lukiyanchuk, B.; Liew, T. Y. F.; Hong, M. H. *Nanotechnology* **2011**, *22*, 245204.
- (97) Fan, J. A.; Wu, C.; Bao, K.; Bao, J.; Bardhan, R.; Halas, N. J.; Manoharan, V. N.; Nordlander, P.; Shvets, G.; Capasso, F. *Science* **2010**, *328*, 1135–1138.
- (98) Luk'yanchuk, B.; Zheludev, N. I.; Maier, S. A.; Halas, N. J.; Nordlander, P.; Giessen, H.; Chong, C. T. *Nat. Mater.* **2010**, *9*, 707–715.
- (99) Brandl, D. W.; Mirin, N. A.; Nordlander, P. *J. Phys. Chem. B* **2006**, *110*, 12302–12310.
- (100) Enoch, S.; Quidant, R.; Badenes, G. *Opt. Express* **2004**, *12*, 3422–3427.
- (101) Alegret, J.; Rindzevicius, T.; Pakizeh, T.; Alaverdyan, Y.; Gunnarsson, L.; Kall, M. *J. Phys. Chem. C* **2008**, *112*, 14313–14317.
- (102) Brown, R. J. C.; Milton, M. J. T. *J. Raman Spectrosc.* **2008**, *39*, 1313–1326.
- (103) Fu, C. Y.; Koh, Z. Y.; Kho, K. W.; Dinish, U. S.; Praveen, T.; Malini, O. *Proc. SPIE* **2009**, *7397*, 739717.
- (104) Lin, X. M.; Cui, Y.; Xu, Y. H.; Ren, B.; Tian, Z. Q. *Anal. Bioanal. Chem.* **2009**, *394*, 1729–1745.
- (105) Gunnarsson, L.; Bjerneld, E. J.; Xu, H.; Petronis, S.; Kasemo, B.; Kall, M. *Appl. Phys. Lett.* **2001**, *78*, 802–804.
- (106) George, V.; Jenkins, T. F.; Leggett, D. C.; Cragin, J. H.; Phelan, J.; Oxley, J.; Pennington, J. *Proc. SPIE* **1999**, *7310*, 258–269.
- (107) Meisenheimer, J. *Justus Liebigs Ann. Chem.* **1902**, *323*, 205–246.
- (108) Sylvia, J. M.; Janni, J. A.; Klein, J. D.; Spencer, K. M. *Anal. Chem.* **2000**, *72*, 5834–5840.
- (109) Jarvis, R. M.; Brooker, A.; Goodacre, R. *Faraday Discuss.* **2006**, *132*, 281–292.
- (110) Jarvis, R. M.; Goodacre, R. *Anal. Chem.* **2004**, *76*, 40–47.
- (111) Premasiri, W. R.; Moir, D. T.; Klempner, M. S.; Krieger, N.; Jones, G.; Ziegler, L. D. *J. Phys. Chem. B* **2005**, *109*, 312–320.
- (112) Premasiri, W. R.; Moir, D. T.; Klempner, M. S.; Ziegler, L. D. *Surface Enhanced Raman Scattering of Microorganisms*; Oxford University Press: New York, 2007.
- (113) Guicheteau, J.; Christesen, S. D. *Proc. SPIE* **2006**, *6218*, G2180–G2180.
- (114) Guzelian, A. A.; Sylvia, J. M.; Janni, J. A.; Clauson, S. L.; Spencer, K. M. *Proc. SPIE* **2002**, *4577*, 182–192.
- (115) Kahraman, M.; Yazici, M. M.; Sahin, F.; Culha, M. *Langmuir* **2008**, *24*, 894–901.
- (116) Liu, T.-T.; Lin, Y.-H.; Hung, C.-S.; Liu, T.-J.; Chen, Y.; Huang, Y.-C.; Tsai, T.-H.; Wang, H.-H.; Wang, D.-W.; Wang, J.-K.; et al. *PLoS One* **2009**, *4*, e5470.
- (117) Liu, Y. L.; Chen, Y. R.; Nou, X. W.; Chao, K. L. *Appl. Spectrosc.* **2007**, *61*, 824–831.
- (118) Marotta, N. E.; Bottomley, L. A. *Appl. Spectrosc.* **2010**, *64*, 601–606.
- (119) Premasiri, W. R.; Gebregziabher, Y.; Ziegler, L. D. *Appl. Spectrosc.* **2011**, *65*, 493–499.
- (120) Zeiri, L.; Bronk, B. V.; Shabtai, Y.; Eichler, J.; Efrima, S. *Appl. Spectrosc.* **2004**, *58*, 33–40.
- (121) Patel, I. S.; Premasiri, W. R.; Moir, D. T.; Ziegler, L. D. *J. Raman Spectrosc.* **2008**, *39*, 1660–1672.
- (122) Wold, S.; Esbensen, K.; Geladi, P. *Chemometr. Intell. Lab.* **1987**, *2*, 37–52.
- (123) Boriskina, S. V.; Reinhard, B. M. *Proc. Natl. Acad. Sci. U.S.A.* **2011**, *108*, 3147–3151.
- (124) Boriskina, S. V.; Reinhard, B. M. *Opt. Express* **2011**, *19*, 22305–22315.